CMIP5 multi-model analyses of projected oceanic response to global warming: North Pacific sea-level rise and equatorial upwelling reduction

（海洋の地球温暖化応答に関する CMIP5 モデルの解析：北太平洋の海面水位上昇と赤道湧昇弱化）

Thesis for a Doctorate

Mio Terada

寺田美緒

Department of Natural History Sciences, Graduate School of Science,

Hokkaido University

北海道大学大学院理学院　自然史科学専攻

March 2019

Abstract

This thesis consists of an analysis of a sea level rise in the North Pacific and an upwelling change along the equator in response to global warming, with emphases on the three-dimensional structure of subsurface ocean. These investigations are important because sea level rise will alter the habitability of coastal regions and equatorial upwelling change has potentials to alter the El Niño through the non-uniform warming of sea surface temperature and to influence ocean deoxygenation. The outputs from the Coupled Model Intercomparison Project Phase 5 (CMIP5) are used and the multi-model ensemble (MME) mean along with differences among models are analyzed in this study.

Future changes in the dynamic sea level (DSL), which is defined as sea level deviation from the global mean sea level, is investigated over the North Pacific, by analyzing data from 30+ CMIP5 models under Representative Concentration Pathway (RCP) 8.5 and RCP4.5 until 2300. The study provides a more comprehensive description of DSL responses to the global warming in this region than previous studies, by using surface and subsurface data. The DSL changes in the North Pacific are characterized by a DSL rise in the western North Pacific around the Kuroshio Extension (KE), consistent with previous studies. Subsurface density analysis indicates that DSL rise around the KE is associated with a decrease in density of subtropical mode water (STMW) and with a northward KE migration. The former is more effective between 2000 and 2100 for both RCP4.5 and RCP8.5 and the latter is more effective between 2100 and 2300 for RCP8.5. The STMW density decrease is related to a large heat uptake to the south and southeast of Japan, while the northward KE migration is associated with the poleward shift of the wind stress field. These features are commonly found in multi-model ensemble (MME) means, and also explain differences among the climate models.

The equatorial upwelling change in the Pacific and Atlantic Oceans is investigated using data from 24 CMIP5 models for RCP8.5 scenario until 2100. Three-dimensional velocity components of CMIP5 multi-models are used for the first time in an upwelling study, and allow to divide upwelling velocities into diapycnal and isopycnal velocities. This analysis, combined with inter-model regression, revealed that both the MME mean and the inter-model variability in the upwelling change in the eastern equatorial Pacific, where strong upwelling change occurs, are explained by two mechanisms. One is that the diapycnal upwelling decreases near the surface associated with the weakened Ekman divergence. The other is that the isopycnal upwelling decreases at depths of 75-200 m around the core of the equatorial undercurrent (EUC) due to the EUC flattening. Both the weakened Ekman divergence and the EUC flattening are induced by the locally weakened trade wind over the eastern Pacific basin. In the equatorial Atlantic, both the MME mean change and the inter-model variability of upwellings are significantly related to the weakened trade wind and enhanced stratification although these drivers are not independent. The results for the Pacific Ocean imply that future upwelling reduction may impact the sea surface temperature and marine ecosystem by different mechanisms. The rapid warming of sea surface temperature in the eastern basin may be related to the near surface diapycnal upwelling reduction, while the decrease of net community production, which often measured by marine export production at a depth of 100 m, may be related to the isopycnal upwelling reduction.

Table of Contents

Chapter 1

General Introduction

Global warming due to increasing greenhouse-gas concentrations has become a principal scientific and socioeconomic concern. The Fifth Assessment Report of the Intergovernmental Panel on Climate Change (IPCC-AR5) released in 2013 indicates that global mean surface temperature shows a warming of about 0.78 ℃ over last 150 years (Hartmann et al. 2013), and it will continue to increase to about 3.7 ℃ until 2100 under the highest emission scenario (Collins et al. 2013). This rapid warming influences climate, ecosystem, and societies around the globe.

Among many oceanic responses to global warming, sea level rise, ocean deoxygenation and ocean acidification pose serious threat to our society, and sea-surface temperature changes can play important role in characterizing future climate. Sea level rise has the potential to alter the habitability of coastal regions (Nicholls et al. 2008). Ocean deoxygenation and acidification will substantially impact on marine ecosystem and consequently on fisheries (Keeling et al. 2010; Gruber 2011). Non-uniform SST warming will cause atmospheric circulation changes (Jia et al. 2016) and will modulate interannual climate variability such as El Niño (Cai et al. 2014; Chen et al. 2015). To understand future changes of these oceanic responses would be very beneficial for the scientific community as well as policy makers. In order to better understand these future responses, it is important to know three dimensional oceanic changes in physical variables including circulations and water mass formations. This thesis aims to understand the mechanism of the ocean response to the global warming, targeting the sea level rise in the North Pacific and upwelling change along the equator. The sea level change is determined by the changes of subsurface density structure which is related to

ocean circulation and water mass formations. The equatorial upwelling change, which may impact substantially equatorial SST and ocean deoxygenation, closely links to the vertical structure of ocean circulation and density along the equator.

Future changes in atmospheres and oceans are projected by global warming experiments of climate models. For these experiments, the concentration of greenhouse gases, aerosols, ozone, and land uses are prescribed as future scenarios. Four scenarios are prepared for the Coupled Model Intercomparison Project Phase 5 (CMIP5) established under the World Climate Research Program (WCRP), and are referred to as the Representative Concentration Pathways (RCPs). These RCP scenarios as well as the scenarios prepared for one generation older CMIP, i.e., CMIP3, were used in the IPCC-AR5. We analyze outputs from more than 30 CMIP5 models for the Multi-model ensemble (MME) mean and inter-model variability that represents uncertainty. The MME mean of CMIP model outputs under present climate generally agree better with observations than the results from individual models (e.g., Boer 2009; Luo et al. 2009; Meinshausen et al. 2011). However, the assessment of future risks of climate change requires not only mean projections but also an estimate of the associated uncertainty ranges because the response of atmosphere and ocean to global warming has a considerable inter-model variability. In this study, we investigate MME mean future response of sea level and upwelling combined with their inter-model variability.

In IPCC-AR5, the future global mean sea-level rise in the 2081–2100 period, relative to the 1986–2005 period, is estimated as 0.47 m (0.32–0.63 m of 90% likely range) and 0.63 m (0.45–0.82 m of 90% likely range) for the middle and high greenhouse-gas emission scenarios of RCP4.5 and RCP8.5, respectively (Church et al. 2013). The sea level changes due to the global warming are not geographically uniform and show

substantial differences among regions. The dynamic sea level is the major factor of this regional changes in sea level (Slangen et al. 2014). Such spatial dependency of sea level change attracts much attention, as shown by the fact that one of the grand challenges of WCRP is “regional sea level change and coastal impacts”. Thus, it is important to understand the mechanisms of sea level change in each region. In chapter 2, we analyze the dynamic sea level, which defined by sea level relative to its global mean of climate model outputs, until 2300 in the western North Pacific where the projected dynamic sea level change is relatively large.

Upwelling along the equator is projected to weaken in the Pacific and western Atlantic until 2100 in CMIP3 climate model until 2100 (Vecchi and Soden 2007). The equatorial upwelling is a key aspect of the El Niño because a weak upwelling results in high SSTs in the eastern equatorial Pacific (McPhaden 1999). The frequency of extreme El Niño events will increase in the warmer climate associated with the rapid warming over the eastern equatorial Pacific (Cai et al. 2014), underlining the importance of understanding how equatorial upwelling respond to the global warming. The equatorial upwelling change is also important for dissolved oxygen change. The upwelling brings nutrient-rich deep water to the near-surface euphotic zone, and enhances biological productivity, which reduces oxygen at depth through biological oxygen consumption. Therefore, understanding of future upwelling change is meaningful for both the physical climate and marine ecosystem. However, the mechanism of equatorial upwelling change has not been fully understood yet. In chapter 3, we analyze the mechanisms of future equatorial upwelling change in the Pacific and Atlantic until 2100.

Chapter 2

Projected sea level rise, gyre circulation and water mass formation in the western North Pacific

2.1. Introduction

Sea-level rise due to global warming is an important issue for human society (see, among others, Lowe and Gregory 2006; Nicholls et al. 2014; Timmermann et al. 2010; Willis and Church 2012). In the Fifth Assessment Report of the Intergovernmental Panel on Climate Change (IPCC-AR5), the future global mean sea-level rise in the 2081–2100 period, relative to the 1986–2005 period, is estimated as 0.47m (0.32–0.63m of 90% likely range) and 0.63m (0.45-0.82m of 90% likely range) for the middle and high greenhouse-gas emission scenarios in Representative Concentration Pathways (RCP) 4.5 and RCP8.5, respectively (Church et al. 2013). An updated assessment by Slangen et al. (2014) suggested higher values: 0.54 m for RCP4.5 and 0.71 m for RCP8.5. Because of continued ocean warming and further melting of the Greenland ice sheet, the global mean sea-level rise continues even when greenhouse-gas concentration is stabilized (Church et al. 2013).

Sea-level rise can be expressed as the sum of the global mean sea-level and a regional sea-level correction defined by the deviation of sea level in the region from the global mean. Regional sea-level change is characterized by the gravity adjustment of land-ice melt (Slangen et al. 2014), terrestrial water storage changes resulting from groundwater depletion (Wada et al. 2012), uplifting of the solid earth due to land-ice mass change (Mitrovica et al. 2011), long term glacial isostatic adjustment (Peltier 2004), non-uniform heat uptake by the ocean (e.g., Lowe and Gregory 2006; Suzuki and Ishii

2011b), and variation of ocean circulation (e.g., Gregory et al. 2001; Yin et al. 2010). Among these components, the last two involve complex dynamic and thermodynamic responses of the ocean to atmospheric forcing, and the difference in sea-level relative to the global mean attributable to these components is called the dynamic sea level (hereinafter, DSL) (e.g., Yin et al. 2010; Zhang et al. 2014). Better understanding of DSL for individual basins is needed for better understanding of sea-level rise issues. In this paper, we study future changes in DSL due to ocean properties (i.e. non-uniform heat uptake and variation of ocean circulation) for the North Pacific.

DSL change over the North Pacific due to global warming is characterized by relatively large sea-level rise in the western North Pacific to the east of Japan. This feature is commonly found in the multi-model ensemble (MME) mean of CMIP3 (Pardaens et al. 2010; Yin et al. 2010; Sueyoshi and Yasuda 2012; Zhang et al. 2014) as well as that of CMIP5 (Yin 2012; Church et al. 2013; Slangen et al. 2014). Since the location of the localized sea-level rise roughly corresponds to the Kuroshio and the Kuroshio Extension (KE), most previous studies have suggested that the rise is related to these currents (Yin et al. 2010; Sueyoshi and Yasuda 2012; Zhang et al. 2014; Liu et al. 2016). Analyzing multiple models of CMIP3, Sueyoshi and Yasuda (2012) reported that the meridional migration and strengthening of the KE each contribute to the regional sea-level change, but these two modes of the KE change occur differently in different models. The northward migration of the KE is associated with the northward shift of the latitude of zero Sverdrup stream function (SSF), which gives the boundary between the subtropical and subpolar gyres of wind-stress-forced circulations in linear models. This is consistent with another CMIP3 analysis by Zhang et al. (2014) and downscaling of three CMIP5 models by Liu et al. (2016). The poleward shift of the zero-

SSF line is closely associated with the northward move of the Aleutian Low (Sueyoshi and Yasuda 2012), and is probably related to the northward expansion of the mean atmospheric circulation, including the Hadley cell (Miller et al. 2006, Rauthe et al. 2004, Collins et al. 2013).

In addition to wind forcings, anomalous heat flux to the ocean can be important in localized sea-level rise in the western North Pacific. Using a series of experiments with a climate model, Suzuki and Ishii (2011a) suggested that large heat uptake, via surface heat flux, in the subtropical mode water (STMW) lowers density of that water mass, resulting in a larger sea-level rise over it. This explanation is consistent with an earlier modeling experiment by Lowe and Gregory (2006). Furthermore, Suzuki and Ishii (2011b) reported that warming and freshening of STMW has played an important role in sea-level rise around the subtropical gyre in the North Pacific over the last three decades by using gridded temperature and salinity data from Ishii and Kimoto (2009).

Further studies are important to better understanding of future DSL changes over the North Pacific. The potential role of heat uptake of STMW has not been investigated in previous multi-model analyses. Moreover, few previous studies of DSL change over the North Pacific using multi-model data of CMIP3 or CMIP5 have analyzed the differences among models. The study by Sueyoshi and Yasuda (2012) is a notable exception, but that analysis is limited to only the 21st century under the middle scenario of the IPCC Special Report on Emission Scenarios (SRES) A1B and does not consider subsurface density and velocity fields. Therefore, expanding analysis to multiple senarios and to a longer time duration (up to the 23rd century, for which some of CMIP models are available) and including subsurface density and velocity fields will clearly advance understanding of sea-level rise. Toward that end, the purpose of this study is to

provide a more comprehensive description and an improved mechanism for assessment of future DSL changes over the North Pacific by analyzing model dependency using multiple climate models of CMIP5. In this study, we analyze both the middle scenario (RCP4.5) and the high scenario (RCP8.5) until the 23rd century, using the outputs of more than 30 climate models for the 21st century. This is more than double the 15 models used by Sueyoshi and Yasuda (2012) the 11 models used by Zhang et al. (2014).

2.2. Data and Methods

The outputs used in this study, which come from climate models participating in CMIP5 (Taylor et al. 2012), are obtained mainly through the Program for Climate Model Diagnosis and Intercomparison (http://cmip-pcmdi.llnl.gov/cmip5/). We used model outputs for the historical experiment up to December 2005 and those for the high- and medium-emissions scenarios of RCP8.5 and RCP4.5, respectively, for January 2006 to December 2300. Outputs of RCP2.6 and RCP6.0 are not analyzed in this study because of the relatively smaller number of available models. Greenhouse-gas concentration and thus radiative forcing stabilizes shortly after 2100 in RCP4.5 (Thomson et al. 2011), and in 2240 in RCP8.5 (Liddicoat et al. 2012). We used outputs of 34 (32) models for RCP8.5 (RCP4.5) until 2100 and of 6 models until 2300. Heat flux data (hfds from CMIP5) are available to the authors from the 23 (9) listed models for RCP8.5 (RCP4.5). We used only the first ensemble of each model so as to treat all models equally. All model outputs are interpolated to a common horizontal grid with $1° \times 1°$ resolution for estimating the MME, and the three-dimensional temperature and salinity data are also interpolated to a common set of 28 vertical levels.

The DSL was defined as the sea level relative to the global mean sea level of CMIP5 models (zos from CMIP5). As mentioned above, DSL includes neither glacial

isostatic adjustment nor gravitational adjustment of land-ice melt and change in land water storage. The inverted barometer effect is not considered because the DSL change related to atmospheric pressure change is much smaller than the steric and DSL change (Slangen et al. 2014).

To understand how sea-level changes are related to density changes at depth, the contribution of the steric component to DSL change is estimated. Sea level can be generally decomposed into steric and mass components (Yin et al. 2010; Zhang et al. 2014; Liu et al. 2016). The sea-level differences due to the steric effect between two epochs ($\Delta\eta$) is given by using the hydrostatic balance:

$$\Delta\eta = -\frac{1}{\rho_0}\int_{h_{REF}}^{0} \Delta\rho dz \qquad (2.1)$$

where $\Delta\rho$ is the in-situ density difference, h_{REF} is the reference depth and ρ_0 is the reference density. The reference depth is set to 2000 m, and the reference density is set to 1025 kg/m3. To understand the density changes corresponding to DSL, we introduce local density, which is defined by the density relative to the global mean density at each depth. This approach allows us to examine how DSL is related to the three-dimensional density structure at each depth in more detail than allowed by the approach employed by Yin et al. (2010), who defined local steric sea-level rise after calculating steric sea-level by vertical integration of densities.

We also calculate the geostrophic velocities using in-situ densities, calculated from temperature and salinity, and sea surface heights on a 1° × 1° grid. Surface velocities are obtained from sea surface height with geostrophic balance assumption, and subsurface velocities are calculated by integrating the thermal wind equation from the surface to downward without an assumption of a level of no motion. It is noteworthy that publicly available CMIP5 data have velocity components only in the original coordinate

system of the model, without information on the angles of coordinates relative to the meridian. This makes it difficult to obtain zonal and meridional components of velocities from CMIP5 outputs by coordinate rotation. Despite this, by using geostrophic velocities, we can assess changes in subsurface oceanic circulation.

2.3. DSL and Density changes

The spatial structure of DSL changes differs before and after 2100. Until 2100, changes are characterized by a meridional dipole accompanying DSL rises (falls) in the subtropical (subpolar) gyre in the western North Pacific for both the RCP4.5 and RCP8.5 scenarios (Figs. 2.1a and 2.1b). This is consistent with previous studies using CMIP5 models (Yin 2012; Church et al. 2013; Slangen et al. 2014) and CMIP3 models (e.g., Sueyoshi and Yasuda 2012; Zhang et al. 2014). These patterns are somewhat (completely) different from the DSL change pattern for RCP8.5 (RCP4.5) from 2100 to 2300. For RCP8.5, the strong DSL rise to the east of Japan between 2100 and 2300 is shifted northward from that between 2000 and 2100, exhibiting a monopole pattern over the basin (Fig. 2.1c). The maximal DSL rise between the 20th and 21st centuries is 11 cm, occurring near the KE east of Japan, and is 23 cm between the 21st and 23rd centuries for RCP8.5. In contrast, DSL changes after 2100 for RCP4.5 are very weak around the KE, and slightly positive in the eastern and northern North Pacific (Fig. 2.1d). The changed structure before and after 2100 is not due to different ensemble sizes (30+ vs 6): the pattern of DSL changes before 2100 identified from the MME of six models that are available through the 23rd century is essentially the same as found with a larger number of models used to produce Figs. 2.1a and 2.1b (Figs. 2.1e and 2.1f).

Time series of area-averaged DSL anomaly from the 1971-2000 mean around the KE over 30°–45°N and 145°–170°E are generally consistent with the temporal

evolution of radiative forcing in each scenario. The time series from RCP8.5 exhibits faster and longer lasting increases than seen from RCP4.5 (Fig. 2.2). The DSL anomaly is rather stable during the end of the 20th century and the early 21st century, and then starts increasing before 2050 for both scenarios. These results for 30+ models are statistically robust, because the 5-95% likely range of 30-year mean MME DSL for each periods are smaller than ±10% of its value. The area-averaged DSL anomaly appears to continuously increase until around the end of the 21st century for RCP4.5 and until the end of the 23rd century for RCP8.5, but internal variability from individual model is remained in 6-model MMEs because of the small ensemble size. Since DSL change in RCP4.5 is weak after 2100, we analyze RCP4.5 only before 2100.

The DSL changes shown in Fig. 2.1 are quite well explained by the steric component (Fig. 2.3). Thus, the DSL change over the North Pacific is dominated by the steric sea-level change. This is consistent with the findings of Yin et al. (2010), who showed that the steric component is dominant in the open ocean. To better understand how three-dimensional density changes are related to DSL changes, we examine local density, which is defined as the density relative to the global mean density at each depth, as mentioned in Section 2.2 (Fig. 2.4). We focus our attention to DSL changes east of Japan, where large DSL changes are found until 2100 under both scenarios and until 2300 in the RCP8.5 scenario, as shown in Fig. 2.1. Until 2100, the local density decrease is centered around 30°N between depths of 100 and 300 m (Figs. 2.4a and 2.4c). In this region, the climatological vertical density gradient is weak, as shown by the wider distance between the σ (1000 kg/m3 is subtracted from in-situ density) contours of 25 and 27 kg/m3 for the end of the 20th century, indicating the presence of STMW. This means that the decreases in local density occur in the STMW, locating over the southern

flank of KE and further south. In contrast, after 2100, the local density decrease has its maximum around 39°N, corresponding to the KE axis rather in the STMW region (Fig. 2.4b). The large negative change in local density near the KE axis suggests its northward migration. Although the density decreases in the region of STMW and near the KE axis occur in both the 21st and 22nd–23rd centuries, the density decreases more strongly in the region of STMW than around the KE axis until 2100 under both RCP4.5 and RCP8.5. Furthermore, the density decreases more strongly around the KE axis than in the STMW region after 2100 under RCP8.5. The density decrease in the STMW is accompanied by a temperature increase (not shown), which suggests that heat uptake associated with the STMW plays an important role in DSL change, as suggested by Suzuki and Ishii (2011b). It is interesting to note that Sugimoto et al. (2017) very recently reported that an enhanced warming of the STMW under the global warming may have already occurred over the past six decades.

The MME time series of volume-averaged local density anomaly for the STMW and for the KE axis latitude anomaly exhibit negative and positive trends, respectively (Fig. 2.5). The KE axis latitude is estimated as the center of gravity of eastward geostrophic surface velocity, zonally averaged over 145°–170°E, 25°–50°N with westward velocities being ignored. Before the 2000s, the time series of STMW density anomaly is roughly stable, but the KE axis latitude appears to start migrating northward before 2000.

Next, we investigate whether these relations we found in MME are common for all models, and if so, we determine how strongly each variables can explain the DSL differences among models. Figure 2.6 shows the relation between DSL changes resulting from changes in STMW density and the DSL changes generally in the region of STMW.

The regression slopes are close to unity (1.54 and 1.45 for RCP8.5 and RCP4.5, respectively for 30+ models), and the correlations are strong (r=0.63–0.83), indicating that the local decrease of density in the STMW well explains the DSL rise there for both periods and scenarios. Figure 2.7 shows changes of the KE axis latitude plotted against DSL differences averaged over 145°–170°E, 35°–40°N which contains the KE axis latitudes during the analysis period. The DSL differences are significantly correlated with the northward migration of the KE latitude. The relationship becomes stronger as the greenhouse-gas emissions accumulate (and thus radiative forcing increases) across different scenarios and periods. This is a new finding obtained by the analysis of multiple scenarios until 2300.

The association between DSL changes and velocity changes at depth is a topic of interest for this study. Figure 2.8 shows that the eastward flow increase (decrease) in the northern (southern) side of the KE, independently of scenario and period, is consistent with the northward KE migration. Another interesting feature is that the velocity changes contains signature of shallowing, which is more clearly seen in the vertical profile of the horizontally averaged zonal geostrophic velocity (Fig. 2.9a). This is associated with velocity weakening in deeper levels, probably because of enhanced upper ocean stratification due to surface warming and freshening (Fig. 2.9b).

2.4. Atmospheric forcing

In this section, we analyze heat flux and wind stress to show how external forcings of the ocean cause changes in DSL. We focus particular attention on how these forcings influence density reduction of the STMW and northward migration of the KE, which were documented in the previous section.

First, we examine the downward net heat flux (positive when ocean gains heat),

which may be related to density change of the STMW (Suzuki and Ishii 2011a; Luo et al. 2009). We first calculate the heat flux anomaly in each year by subtracting its mean value of last 30 years in 20th century, and then integrate it from 1971 to 2100 (Figs. 2.10a and 2.10b). The integrated downward heat flux anomaly is large in high latitudes (north of 50°N) and to the south and southeast of Japan. The former causes a large temperature increase in higher latitudes, but this heat uptake contributes less to local density, and thus to DSL, than in lower latitudes because of the nonlinearity of the density equation for sea water. The mid-latitude positive integrated heat flux anomalies are located to the south of the climatological mean negative maximum (i.e., the location of maximum heat loss from the ocean over KE), and negative anomalies occur to the north of the climatological mean negative maximum. This spatial pattern represents northward migration of the heat flux field. It implies a link between the heat flux anomaly and northward migration of the KE. Area-averaged downward net heat flux continually increases south and southeast of Japan until the middle of the 23rd (21st) century for the RCP8.5 (RCP4.5) scenario (Fig. 2.10c).

The relation between changes in downward net heat flux and local density of the STMW is confirmed by analysis of differences among models (Fig. 2.11). Here, we limit our analysis of epochal differences, considering only between the ends of the 20th and 21st centuries because we have only four models for which heat flux data are available until 2300, and this is too few for analysis of the relationship among models. Local density change in the STMW is negatively correlated with integrated downward heat flux anomalies south of Japan. Further investigation revealed that reduced atmospheric cooling in winter contributes more to STMW density decrease than increased atmospheric heating in summer (not shown). This means that anomalous

ocean heat uptake in winter results in lighter water mass in the STMW. As shown in the previous section, the lower density of this water mass is important in producing the maximal sea-level rise to the east of Japan.

The aforementioned possible link between the time-integrated downward heat flux anomaly to the south of Japan and northward KE migration is examined with various climate models (Fig. 2.12). The changes in downward net heat flux are strongly related to meridional migration of the KE axis latitude, with a correlation coefficient of 0.84 (0.95) for RCP8.5 (RCP4.5). This indicates that the northward KE migration is closely related to the anomalous heat flux south of Japan. Since downward heat flux takes its minimum along the KE axis (see contours of Figs. 2.10a and 2.10b), downward net heat flux will be increased (reduced) in the south (north) of its axis when it moves northward. Therefore, KE migration, integrated heat flux anomalies, and density changes of STMW are related. A possible causality is that the KE northward migration accounts for producing lighter water for the STMW through the anomalous ocean heat uptake south of the KE axis until 2100. This chain of causality, however, is not dominant factor for STMW density change, because the correlation between the STMW density change and integrated heat flux anomaly is moderate ($r=-0.45$ in Fig. 2.11a) and because the density decrease of STMW rather than the northward KE migration plays a more important role in DSL changes in the 21st century as mentioned above.

The meridional migration of the KE can be caused by variations of wind distribution because the KE participates in wind-driven circulation over the North Pacific. Figures 2.13a and 2.13b show the differences in zonal wind stress between the 1971–2000 and 2071–2100 periods under RCP8.5 and RCP4.5, respectively. Zonal wind stress is enhanced (weakened) to the north (south) of the climatological maximum zonal

wind, centered around 40°N across the North Pacific, with stronger magnitudes for RCP8.5 than for RCP4.5. This spatial pattern indicates northward migration of the zonal wind stress field, consistent with previous studies (Sueyoshi and Yasuda 2012; Zhang et al. 2014). The wind stress curl field also exhibits northward migration of time-mean pattern, and its change is characterized by an anticyclonic anomalies extending eastward from the east coast of Japan (not shown). The latitude of zonally averaged zonal wind stress maximum moves 1 (0.4) degrees to the north by 2100 in RCP8.5 (RCP4.5). Anomaly time series of the latitude of zero Sverdrup stream function (SSF) at 150° E over the North Pacific (150°E–160°W) exhibit northward movement until roughly the middle of the 21st (23rd) century for RCP4.5 (RCP8.5) (Fig. 2.13c), though internal variability in each model is not averaged out especially in 6-model MME.

Northward migration of the KE is significantly correlated (at the 5% significance) with that of the latitude of zero SSF under RCP8.5 ($r=0.54$, $p<0.01$), but the correlation under RCP4.5 is not significant ($r=0.21$, $p=0.27$) (Fig. 2.14). This means that although the MME indicates that both the KE axis and zero SSF latitude move northward, different KE migrations among models are not well explained by the shift in zero SSF latitude under RCP4.5. The stronger relationship in RCP8.5 relative to RCP4.5 suggests that the uncertainty in RCP4.5 may arise from internal variability of the ocean, though further studies are necessary to clarify this. It is interesting to note that the regression slopes are all shallower than unity, meaning that the northward migration of the KE is smaller than migration of the zero SSF latitude in many models. This migration discrepancy may be due to a strong non-linearity of the KE, although its specific contribution is uncertain.

The northward migration of the SSF field and hence that of the zonal wind

stress is likely influenced by the change of large-scale atmospheric circulation. Figure 2.15 shows the MME changes of sea-level pressure (SLP) over the North Pacific. Between the ends of the 20th and 21st centuries, SLP changes are characterized by decreases in the Bering Sea and increases in the central and western North Pacific between 30°N and 40°N (Figs. 2.15a and 2.15c). This pattern of change in SLP indicates overall deepening and northward shifting of the Aleutian Low, consistent with previous studies (e.g., Sueyoshi and Yasuda 2012; Oshima et al. 2012; Collins et al. 2013; Gan et al. 2017). These changes to the Aleutian Low continue after 2100 and are accompanied by weakening of the subtropical high (Fig. 2.15b). The spatial patterns of changes in SLP are associated with positive trends of the annular modes as well as with poleward expansion of the Hadley circulation (Miller et al. 2006; Rauthe et al. 2004; Collins et al. 2013). These two phenomena may result from global warming (Cheon et al. 2012; Frierson et al. 2007; Hu et al. 2013; Johanson and Fu 2009; Lu et al. 2007; Previdi and Liepert 2007).

2.5. Discussion and Summary

We investigated change in DSL over the North Pacific until 2300 under middle and high greenhouse-gas emission scenarios (RCP4.5 and RCP8.5, respectively) by analyzing MME along with differences among models, including subsurface density and velocity fields, using output from CMIP5 models. This is the first study of subsurface density and velocity fields for the future DSL change in the western North Pacific. Hence, our analysis has provided more comprehensive understanding of future DSL changes.

The DSL changes in the North Pacific are characterized by DSL rise in the western North Pacific around the KE (Fig. 2.1), as reported in previous studies (Yin et al. 2010; Yin 2012; Sueyoshi and Yasuda 2012; Zhang et al. 2014; Church et al. 2013;

Slangen et al. 2014). Around the KE, DSL continues to rise roughly through the 21st century under RCP4.5 and until the end of the 23rd century under RCP8.5, indicating that DSL will continue to change for decades after stabilization of radiative forcing (Fig. 2.2). The localized DSL change around the KE is related to a density decrease of the STMW and to northward migration of the KE (Fig. 2.3). Both of them induce DSL rise in the western North Pacific by 2100 and 2300. Specifically, the density decreases more strongly in the region of STMW than that around the KE axis until 2100 under both RCP4.5 and RCP8.5, whereas the density decreases more strongly around the KE axis than in the STMW region after 2100 under RCP8.5 (Fig. 2.4). The different patterns of density changes between the two periods result in the different spatial distributions of DSL changes by 2100 and 2300. The local density decrease in the STMW and the KE northward migration also explain different DSL changes among models (Figs. 2.6 and 2.7). The KE migration is confirmed by subsurface geostrophic velocity analysis (Fig. 2.8). The KE exhibits not only a simple meridional migration but also a stronger concentration near the surface, probably due to enhanced stratification (Fig. 2.9).

The reduction in STMW density is likely to be caused at least in part by high heat uptake to the south and southeast of Japan, where the Kuroshio and its extension flow (Figs. 2.10 and 2.12). The excess heat flux in this region is very strongly related to the northward migration of the KE (Fig. 2.12). This northward KE shift is forced, at least in part, by changes in wind distribution, and the northward shift of the latitude of zero SSF results in northward shift of the KE (Figs. 2.13 and 2.14). The poleward shift of the wind field is related to the poleward shift of the atmospheric circulation (Fig. 2.15), which is probably related to the poleward expansion of the Hadley circulation. The major features and mechanisms of DSL rise in the western North Pacific between 2000 and

2100 are summarized in Fig. 2.16.

As discussed in Section 2.1, previous studies suggest that the strong DSL rise in the western North Pacific around the KE is due to anomalous heat uptake, mainly due to STMW (Lowe and Gregory 2006; Suzuki and Ishii 2011b), the northward migration of the KE (Sueyoshi and Yasuda 2012; Zhang et al. 2014) or KE intensification (Sueyoshi and Yasuda 2012). Among these three mechanisms, the first and last, anomalous heat uptake by the STMW and KE intensification may be closely associated. This is because the KE strength, defined by Sueyoshi and Yasuda (2012) as the meridional DSL difference between 34°N and 42°N for a 150°–165°E range, is the most likely to be dominated by a change in DSL at 34°N, which is within the meridional range of the STMW (Fig. 2.4). DSL change is much stronger at 34°N than at 42°N (Fig. 2.1), even using the composite difference for models that exhibit strong KE intensification (see Fig. 9 of Sueyoshi and Yasuda 2012). Consequently, we suggest that KE intensification may be better understood as an aspect of the heat uptake of STMW. This means that heat uptake by the STMW and meridional migration of the KE are the two essential mechanisms for DSL changes around the KE, though these two mechanisms are not totally independent, as shown by a significant correlation between the KE meridional migration and excess heat uptake to the south and southeast of Japan (Fig. 2.12).

The DSL changes attributable to these two mechanisms differ substantially among models. Figure 2.17 shows the local density difference for each model in the western North Pacific (145°–170°E) under RCP8.5. Most of the models exhibit local density differences for the STMW, but the magnitudes of the differences have wide variability, consistent with the situation in Fig. 2.5. Furthermore, many models

(specifically, CMCC-CESM, CMC-CM, CMCC-CM5, FGOALS-g2, and IPSL-CM5A-MR) exhibit stronger changes associated with the KE, and some other models (CanESM2, hadGEM2-CC, HadGem2-ES, MIROC-ESM, MIROC-ESM-CHEM, MPI-ESM-MR) exhibit two maxima, corresponding to the STMW and the KE.

The inter-model differences of future response are bringing into question how these large inter-model differences are related to the mean state differences. To address this question, we apply the inter-model singular value decomposition (SVD) analysis that was used by Lyu et al. (2016) to examine the relationship between climatological mean state and interdecadal variability patterns among CMIP5 models. We first derive the departures of each model's DSL averaged for 1971-2000 period and the DSL difference between 1971-2000 and 2071-2100 periods from the MME mean patterns in the North Pacific (120°E-115°W, 20°N-60°N), and then apply the inter-model SVD analysis. The first mode explains only 12% of total variance, and there is no significant co-variation in the western North Pacific where we focus on in this study. Therefore, the inter-model differences in the DSL rise around the KE is not well explained by the mean state difference. Future work is required for the better understanding of the reasons for model differences that would lead to better overall understanding and more certain projections.

Table 2.1. CMIP5 models used in this study. HF indicates that downward net heat flux data (hfds in CMIP5) were available to the authors.

	Model	Country	2100 RCP8.5 (34 models)	2100 RCP4.5 (32 models)	2300 RCP8.5 (6 models)	2300 RCP4.5 (6 models)
A	BCC-CSM1-1	China	✓ (HF)	✓	✓ (HF)	✓
B	CNRM-CM5	France	✓ (HF)	✓	✓ (HF)	✓
C	GISS-E2-R	USA	✓ (HF)	✓	✓ (HF)	✓
D	HadGEM2-ES	UK	✓	✓	✓	✓
E	IPSL-CM5A-LR	France	✓	✓	✓	✓
F	MPI-ESM-LR	Germany	✓ (HF)	✓ (HF)	✓ (HF)	✓ (HF)
G	ACCESS1-0	Australia	✓ (HF)	✓		
H	ACCESS1-3	Australia	✓ (HF)	✓		
I	BCC-CSM1-1-M	China	✓ (HF)	✓ (HF)		
J	CCSM4	USA	✓	✓		
K	CESM1-BGC	USA	✓	✓		
L	CESM1-WACCM	USA	✓	✓		
M	CMCC-CESM	Italy	✓ (HF)			
N	CMCC-CM	Italy	✓ (HF)	✓ (HF)		
O	CMCC-CMS	Italy	✓ (HF)	✓ (HF)		
P	CSIRO-Mk3-6-0	Australia	✓ (HF)	✓		
Q	CanESM2	Canada	✓	✓		
R	FGOALS-g2	China	✓ (HF)	✓ (HF)		
S	FGOALS-s2	China	✓ (HF)	✓		
T	FIO-ESM	China	✓ (HF)	✓		
U	GFDL-CM3	USA	✓	✓		
V	GFDL-ESM2G	USA	✓ (HF)	✓		
W	GFDL-ESM2M	USA	✓	✓		
X	HadGEM2-CC	UK	✓	✓		
Y	IPSL-CM5A-MR	France	✓	✓		
Z	IPSL-CM5B-LR	France	✓	✓		
a	MIROC-ESM	Japan	✓ (HF)	✓ (HF)		
b	MIROC-ESM-CHEM	Japan	✓ (HF)	✓ (HF)		
c	MIROC5	Japan	✓ (HF)	✓		
d	MPI-ESM-MR	Germany	✓ (HF)	✓ (HF)		
e	MRI-CGCM3	Japan	✓ (HF)	✓ (HF)		
f	MRI-ESM1	Japan	✓ (HF)			
g	NorESM1-M	Norway	✓ (HF)	✓		
h	NorESM1-ME	Norway	✓ (HF)	✓		

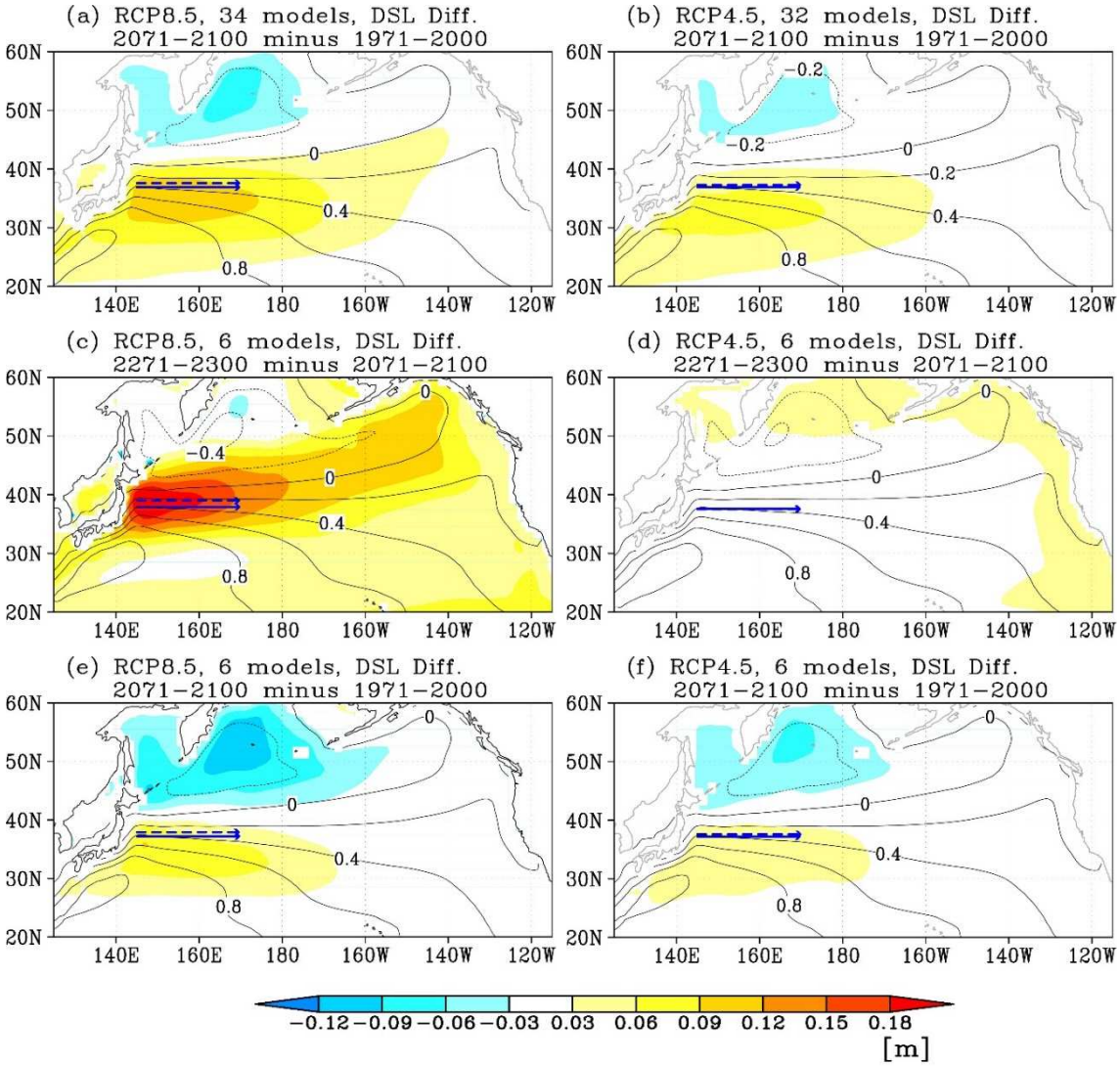

Figure 2.1. DSL differences (color) (a) between 1971–2000 and 2071–2100 periods for 34-model MME under RCP8.5, (b) between 1971–2000 and 2071–2100 periods for 32-model MME under RCP4.5, (c) between 2071–2100 and 2271–2300 periods for 6-model MME under RCP8.5, and (d) between 2071–2100 and 2271–2300 periods for 6-model MME under RCP4.5. Panel (e) and (f) is same as (a) and (b) but for 6-model MME. Contours indicate the mean DSL for the periods of (a, b, d, f) 1971–2000 and (c, d) 2071–2100. Solid (dashed) blue arrows indicate the KE axis latitude for the periods of (a, b, e, f) 1971–2000 (2071–2100) and (c, d) 2071–2100 (2271–2300). The KE axis latitude is estimated as the center of gravity of eastward geostrophic surface velocity, zonally averaged over 145°–170°E, 25°–50°N.

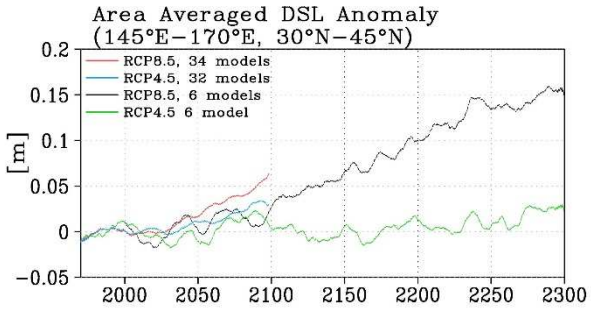

Figure 2.2. Time series of the area-averaged (145°–170°E, 30°–45°N) DSL anomaly from 1971-2000 mean smoothed by applying an 11-year running mean for 34-model MME under RCP8.5 (red), 32-model MME under RCP4.5 (blue), 6-model MME under RCP8.5 (black), and 6-model MME under RCP4.5 (green).

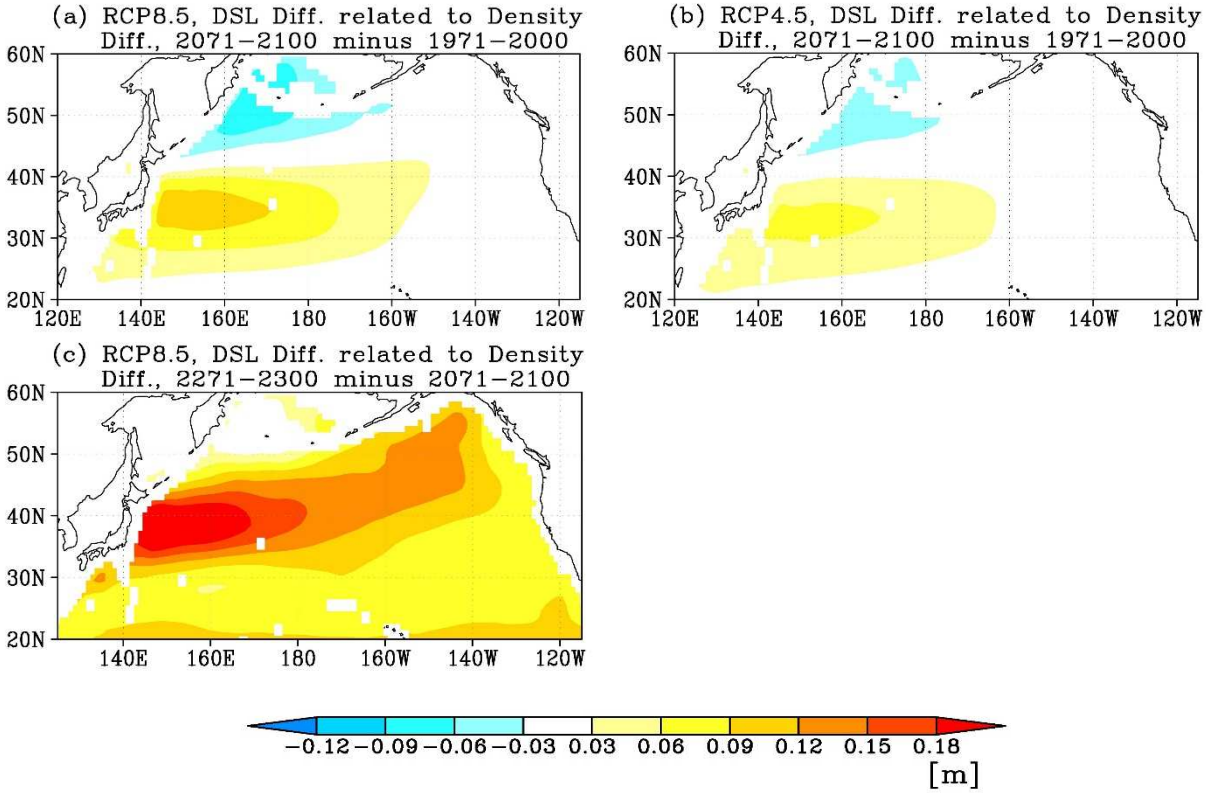

Figure 2.3. Same as Figs. 2.1a–c, but for local steric sea-level differences.

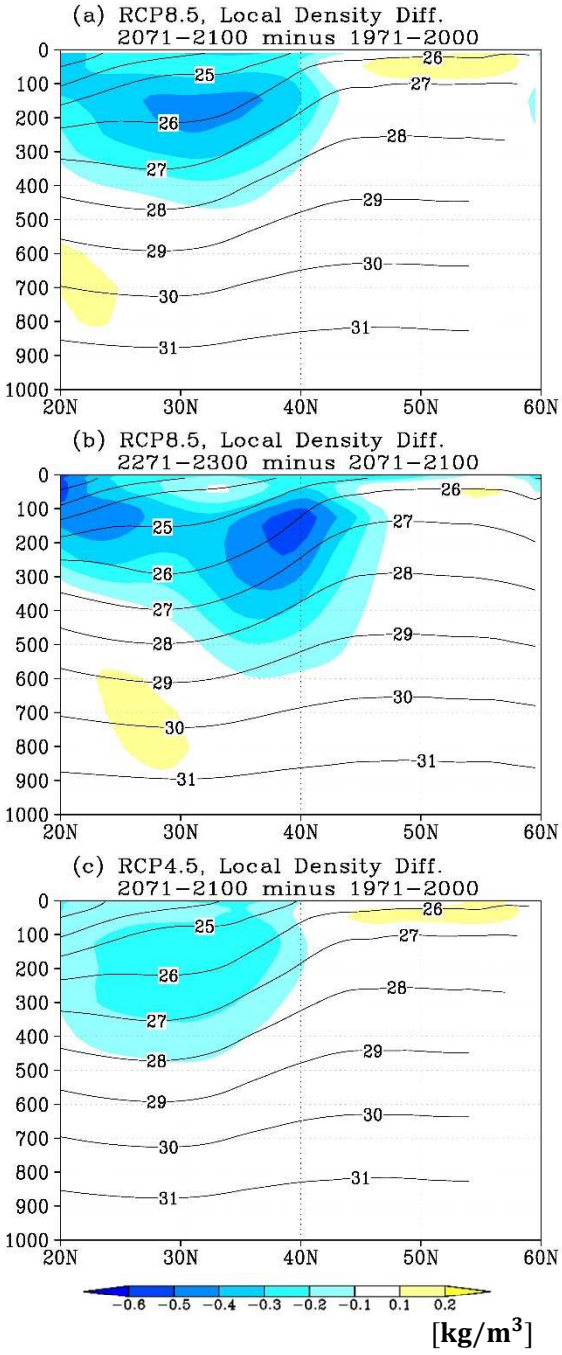

Figure 2.4. Zonally averaged (145°–170°E) local density differences (color) (a) between 1971–2000 and 2071–2100 periods for 34-model MME under RCP8.5, (b) between 2071–2100 and 2271–2300 periods for 6-model MME under RCP8.5, and (c) between 1971–2000 and 2071–2100 periods for 32-model MME under RCP4.5. Local density is defined as the deviation from global mean density at each level (see text). Contours indicate the mean σ for the periods (a,c) 1971–2000 and (b) 2071–2100.

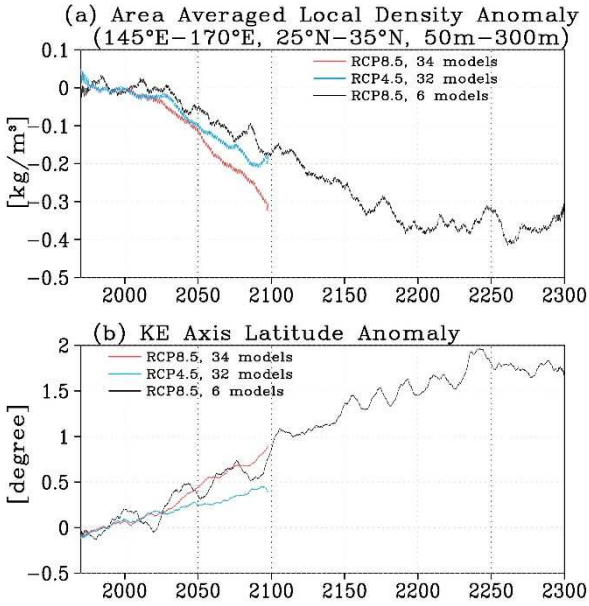

Figure 2.5. Time series of (a) local density anomaly averaged in the STMW region (145°–170°E, 25°–35°N, and depth 50–300 m) and (b) the KE-axis latitude anomaly smoothed by applying an 11-year running mean for 34-model MME under RCP8.5 (red), 32-model MME under RCP4.5 (blue), and 6-model MME under RCP8.5 (black).

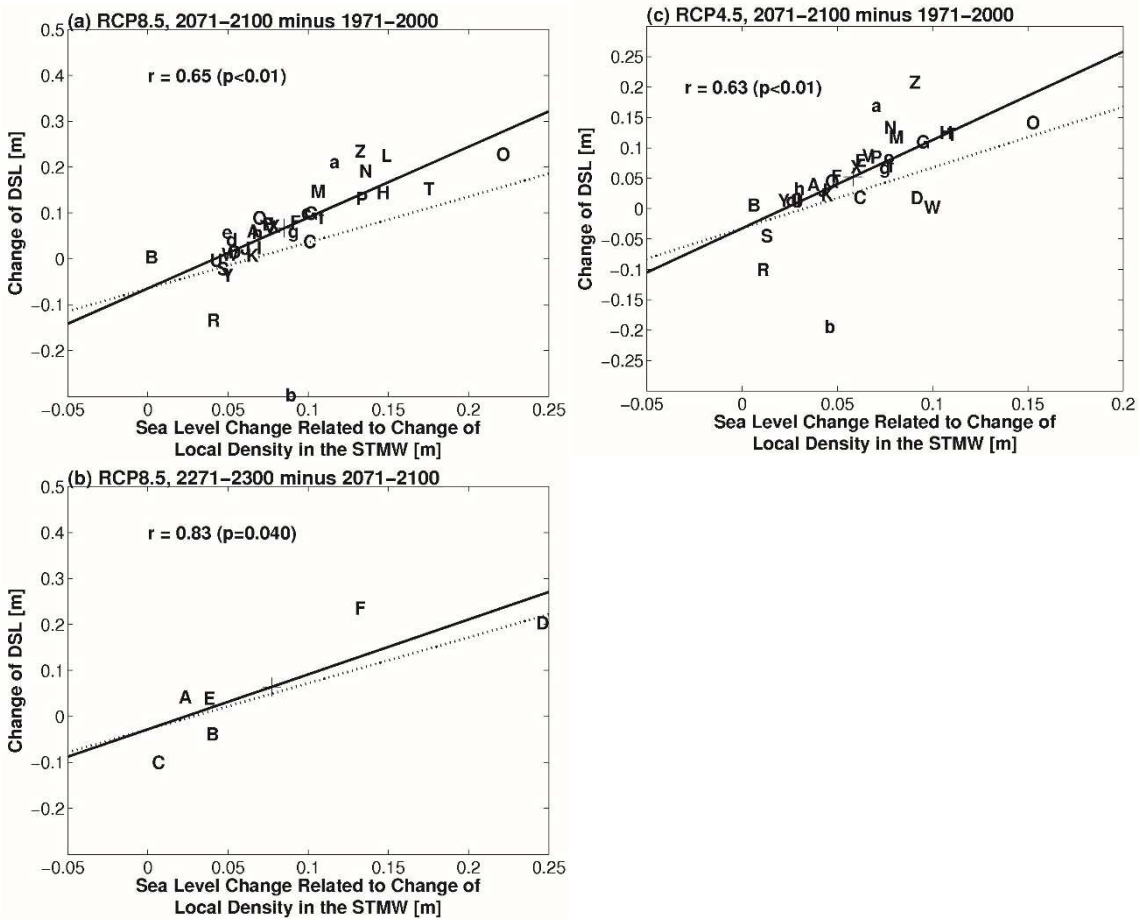

Figure 2.6. Scatter diagram of epoch differences in DSL due to local density averaged in the STMW region (145°–170°E, 25°–35°N, and depth 50–300 m) and DSL over the same domain among climate models. The epochs and scenarios are (a) 1971–2000 and 2071–2100 periods under RCP8.5, (b) 2071–2100 and 2271–2300 periods under RCP8.5, and (c) 1971–2000 and 2071–2100 periods under RCP4.5. The plus symbol (+) and alphabetical letters denote the MME and the models (Table 1), respectively. Correlation coefficients and *p*-values are shown in the panels. Solid lines indicate regression lines, while dotted lines denote the lines of slope 1.

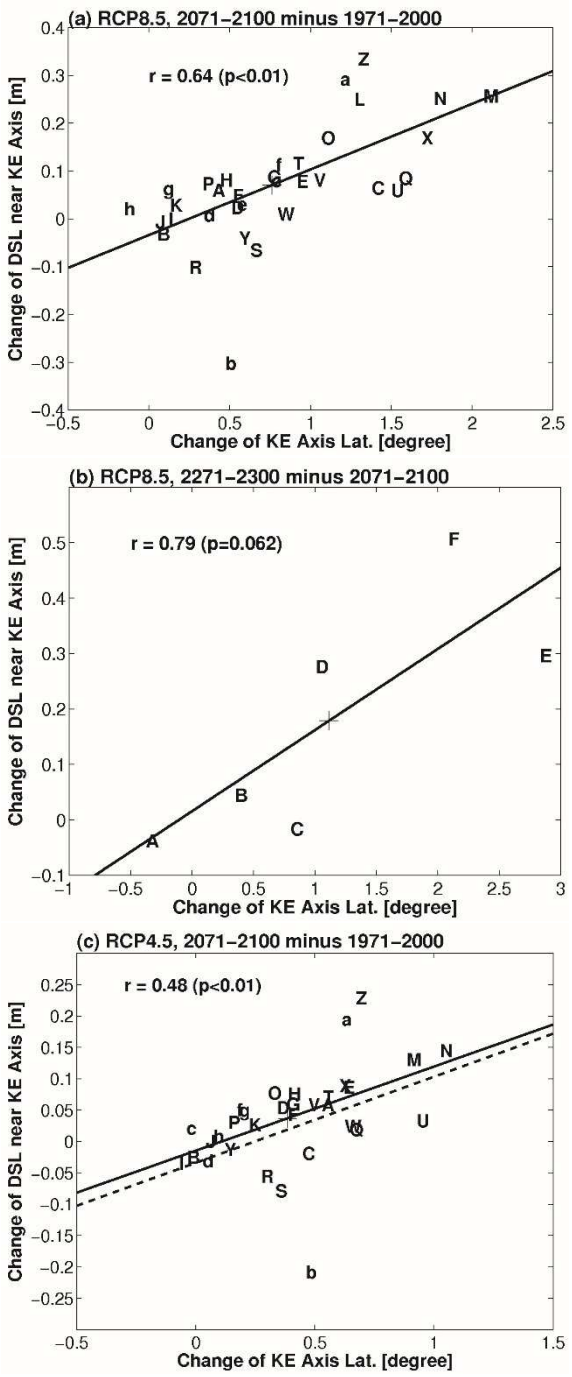

Figure 2.7. As in Fig. 2.6, but for epoch differences of KE axis latitude and DSL around the KE axis (145°–170°E, 35°–40°N) among climate models. The dashed line in (c) is the regression line from (a).

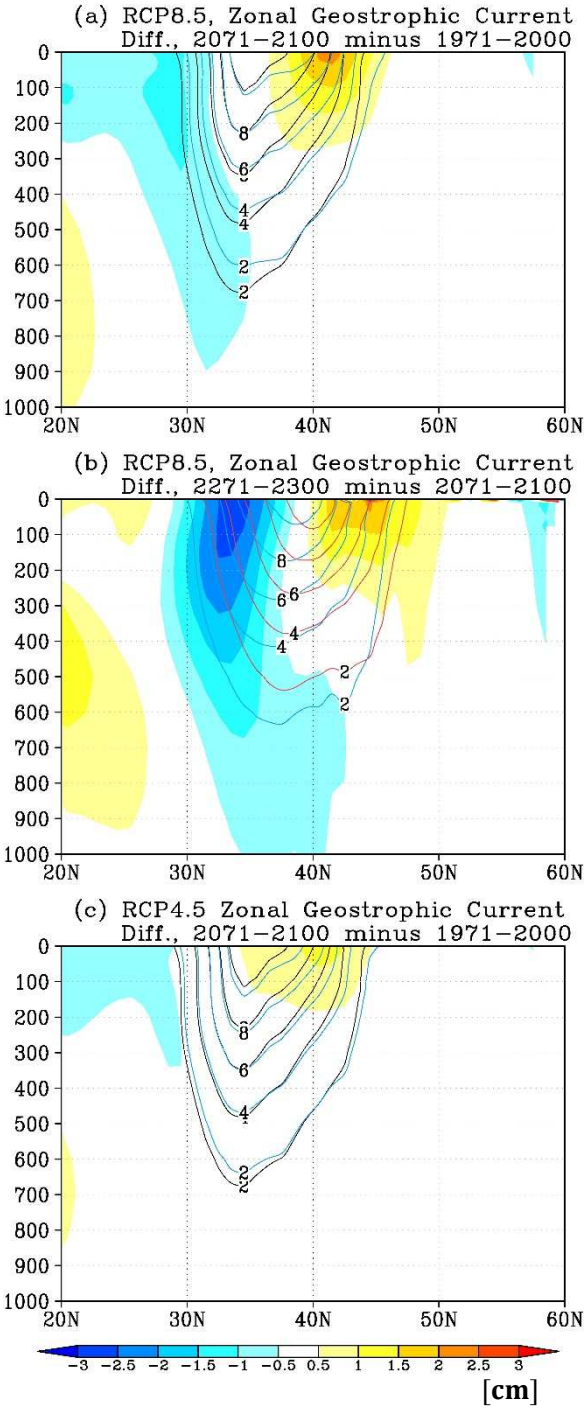

Figure 2.8. Eastward geostrophic current-speed differences (color), calculated using the zonally averaged (145°–170°E) in-situ density and sea level (a) between 1971–2000 and 2071–2100 periods for 34-model MME under RCP8.5, (b) between 2071–2100 and 2271–2300 periods for 6-model MME under RCP8.5, and (c) between 1971–2000 and 2071–2100 periods for 34-model MME under RCP4.5. Black, blue, and red contours indicate the mean zonal geostrophic current speed for the periods 1971–2000, 2071–2100, and 2271–2300, respectively

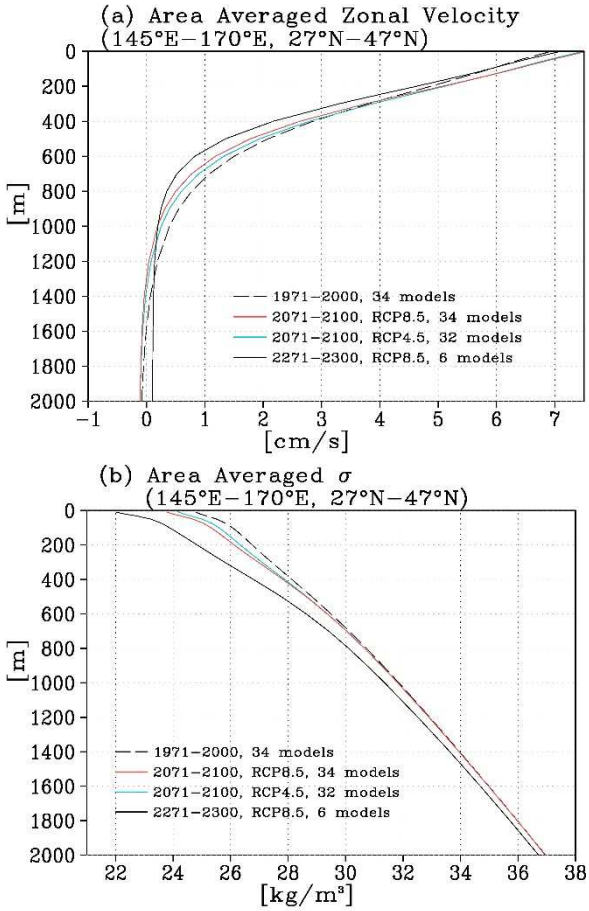

Figure 2.9. Vertical profiles of (a) zonal velocity and (b) σ averaged in 145°–170°E, 27°N–47°N for (black dashed curve)1971–2000 period in the historical experiment , (red curve) 2071–2000 period under RCP8.5, (blue curve) 2071–2000 period under RCP4.5, and (black solid curve) 2272–2300 period under RCP8.5.

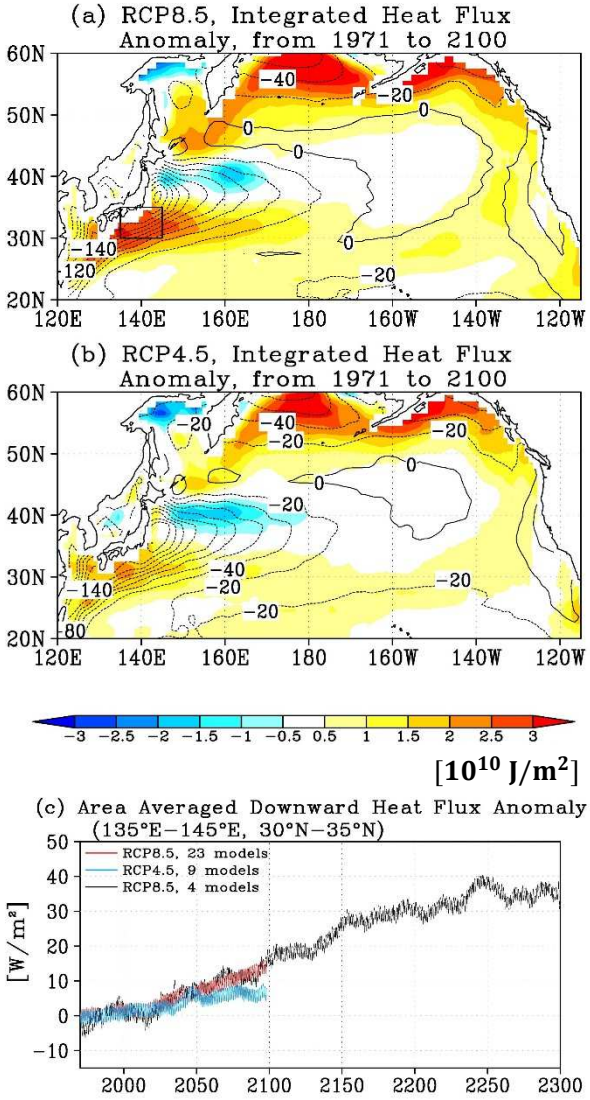

Figure 2.10. Time-integrated downward net heat flux anomaly (color) for (a) 23-model MME under RCP8.5 and (b) 9-model MME under RCP4.5. Panel (c) shows the time series of area-averaged downward net heat flux (130°–160°E, 25°–35°N) anomaly from 1971–2000 mean smoothed by applying an 11-year running mean for the following: (red) 23-model MME under RCP8.5, (blue) 9-model MME under RCP4.5, and (black) 4-model MME under RCP8.5. Contours in panels (a) and (b) indicate the mean downward net heat flux for the period 1971–2000. The domain for area averaging is marked by the box in (a).

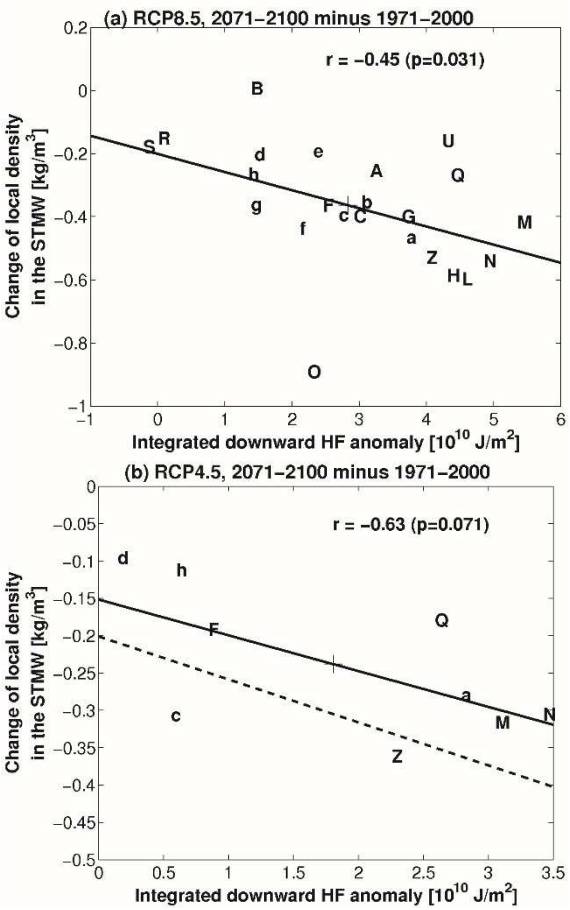

Figure 2.11. Scatter diagram of epoch differences of the local density averaged in the STMW region (145°–170°E, 25°–35°N, and depth 50–300 m) and integrated downward net heat flux averaged south of the KE (130°–160°E, 25°–35°N) among climate models between 1971–2000 and 2071–2100 periods. The scenarios are (a) RCP8.5 and (c) RCP4.5. The plus symbols (+) and alphabetical letters denote MME and the models (Table 1), respectively. Correlation coefficients and *p*-values are shown. Solid lines indicate the regression line from the data points. The dashed line in (b) is the regression line from (a).

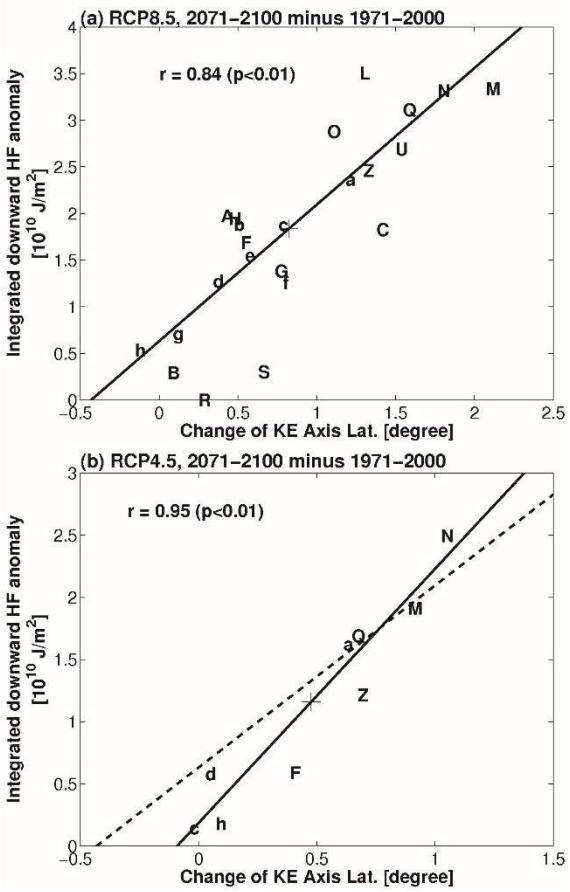

Figure 2.12. As in Fig. 2.11, but for epoch differences of the KE-axis latitude and integrated downward net heat flux averaged south of the KE (135°–145°E, 30°–35°N) among climate models. The dashed line in (b) is the regression line from (a).

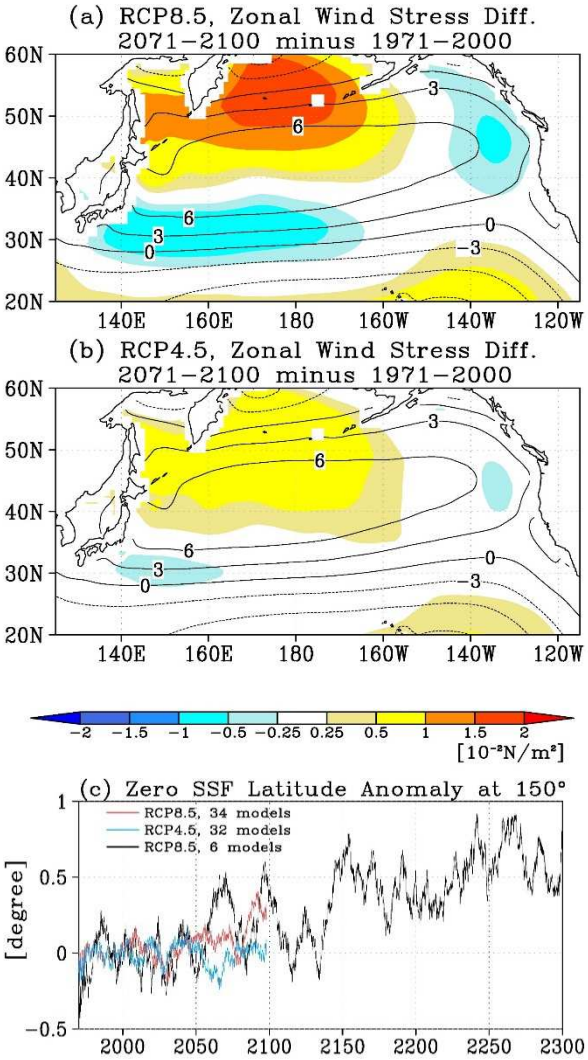

Figure 2.13. Zonal wind stress differences between 1971–2000 and 2071–2100 periods (color) (a) for 34-model MME under RCP8.5 and (b) for 32-model MME under RCP4.5. Contours indicate the mean zonal wind stress for the period 1971–2000. (c) Anomaly time series of the latitude of zero SSF at 150°E relative to 1971–2000 mean smoothed by applying an 11-year running mean for the following: (red) 34-model MME under RCP8.5, (blue) 32-model MME under RCP4.5, and (black) 6-model MME under RCP8.5. The zero SSF line is calculated by zonally integrating wind stress curl westward from the eastern boundary (i.e., Sverdrup Balance).

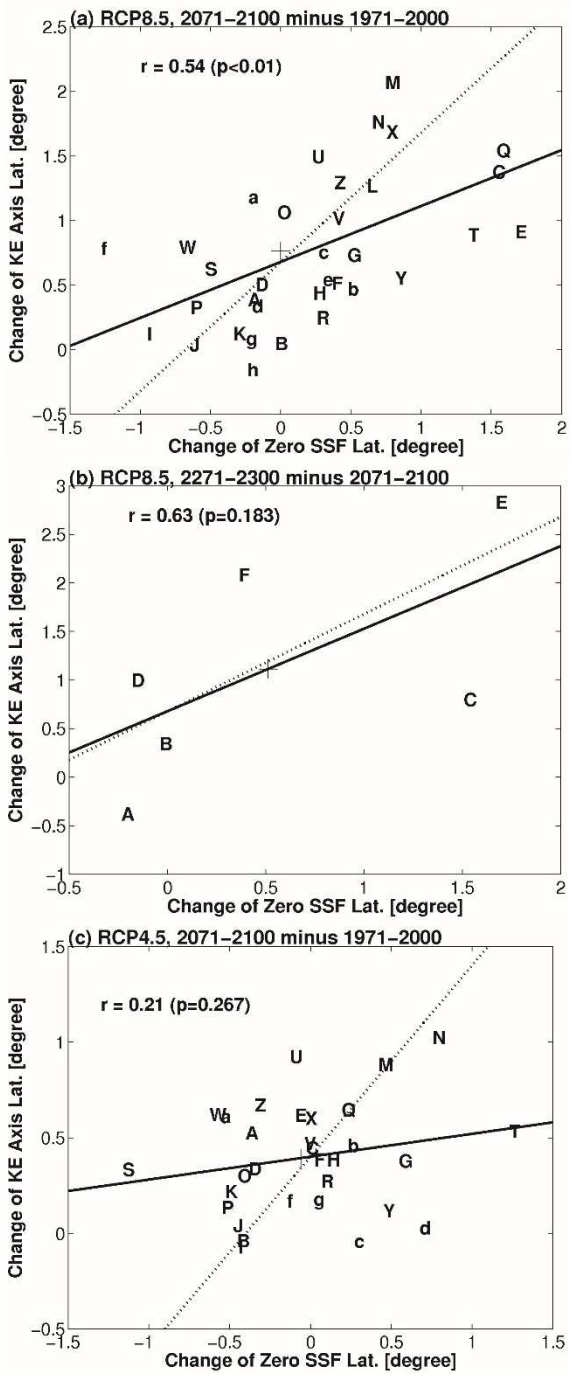

Figure 2.14. As in Fig. 2.6, but for epoch differences of the KE-axis latitude and the latitude of zero SSF at 150°E among climate models. Dotted lines indicate slope 1.

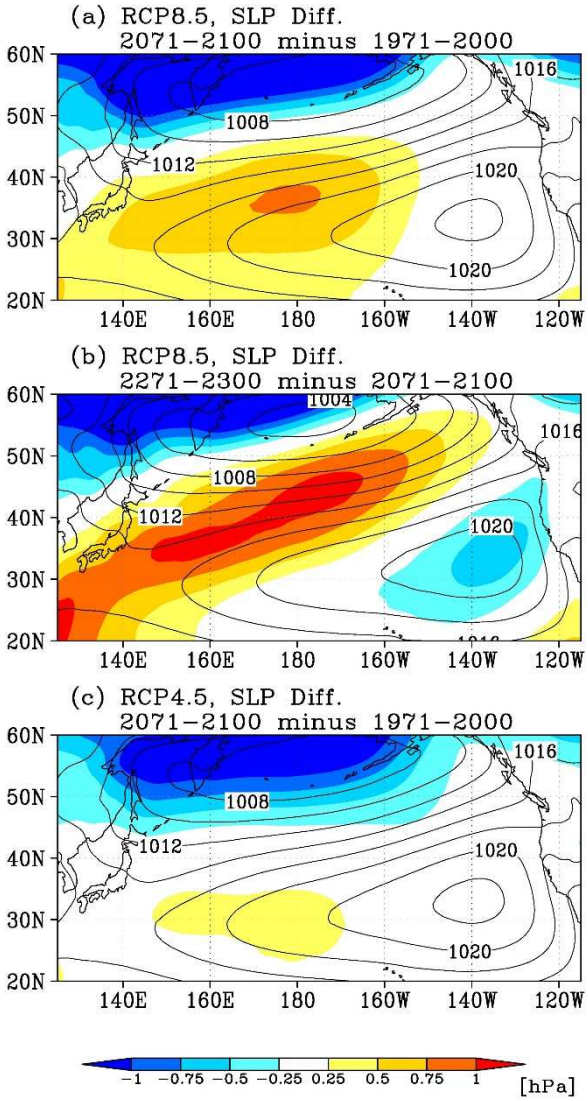

Figure 2.15. Epoch differences of SLP (color) (a) between 1971–2000 and 2071–2100 periods for 34-model MME under RCP8.5, (b) between 2071–2100 and 2271–2300 periods for 6-model MME under RCP8.5, and (c) between 1971–2000 and 2071–2100 periods for 32-model MME under RCP4.5. Contours indicate the mean SLP for the periods (a, c) 1971–2000 and (b) 2071–2100.

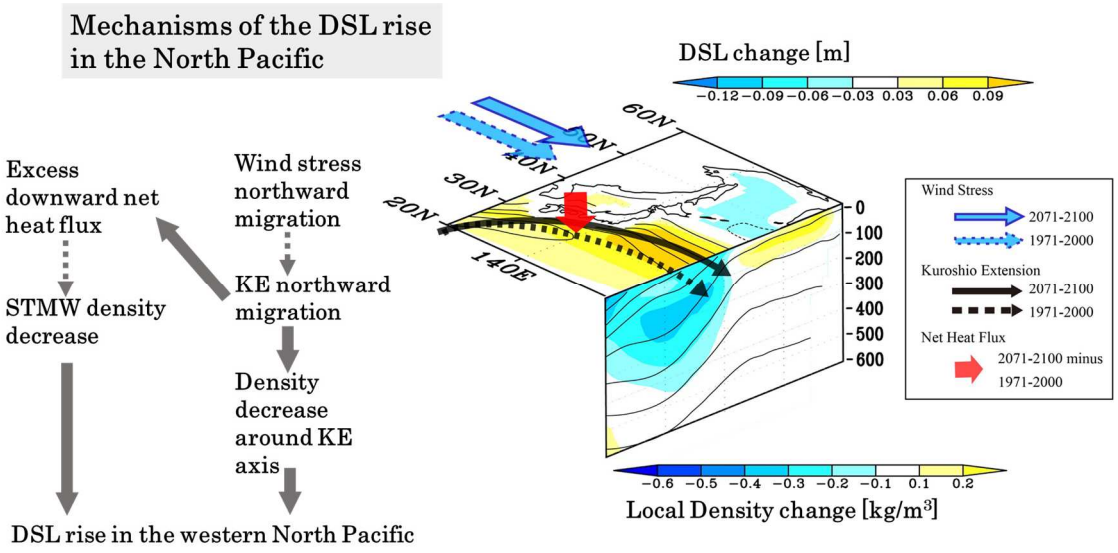

Figure 2.16. Schematic diagram illustrating the mechanism of DSL rise in the western North Pacific. DSL rises around the KE is associated with the density decrease of the STMW and northward KE migration. The STMW density decrease is caused by anomalous downward net heat flux to the south and southeast of Japan, while the northward KE migration is due to the poleward shift of the wind stress field. The excess heat flux is also strongly related to the northward migration of the KE. The solid arrows indicate the inter-model relationships that are significant at 5% significance level for both the RCP4.5 and 8.5, while dashed arrows indicate the relationships that are significant only for RCP8.5 but not for RCP4.5.

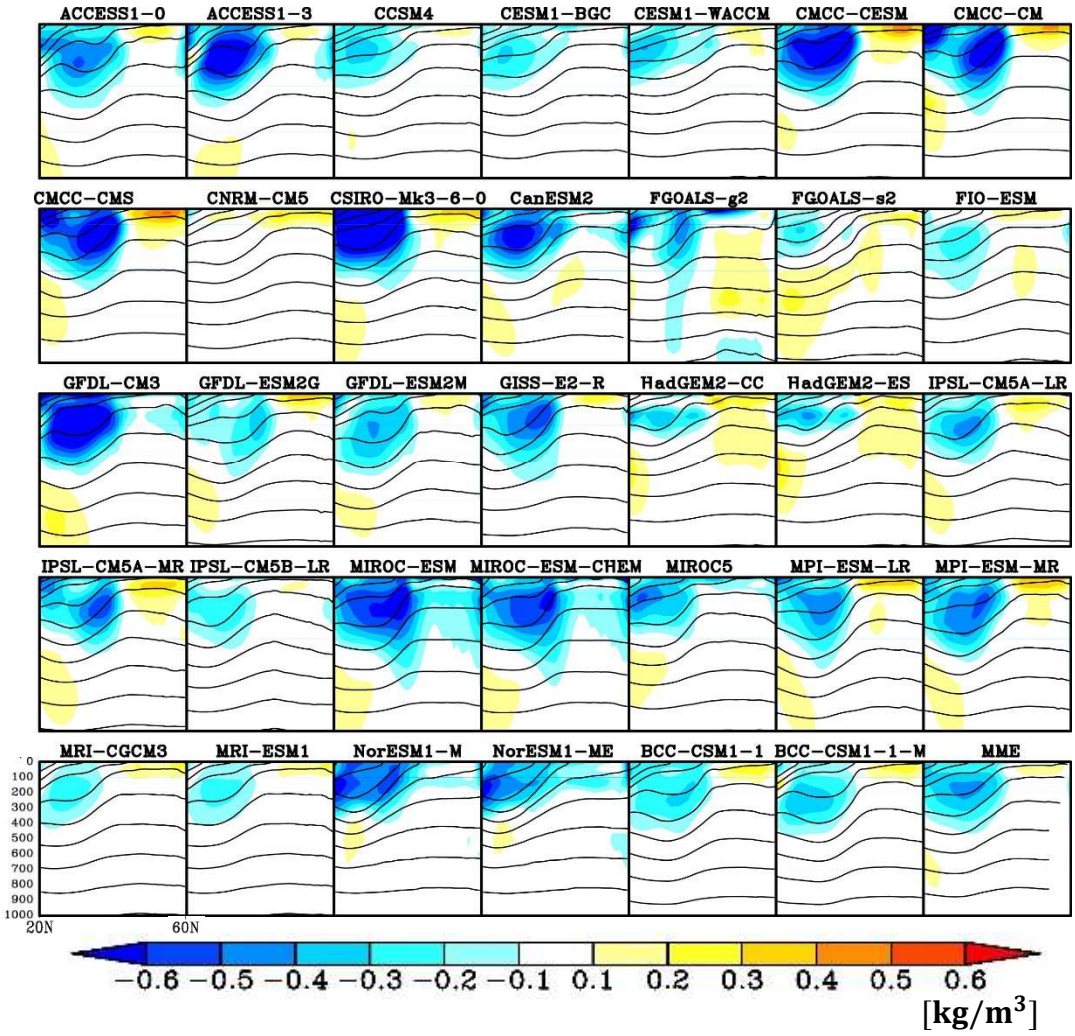

Figure 2.17. Zonally averaged (145°–170°E) local density differences between 1971–2000 and 2071–2100 periods under RCP8.5 for each model (color). Contours indicate the mean σ for the period 1971–2000. MME indicates the MME mean.

Chapter 3

Mechanisms of future equatorial upwelling change

3.1. Introduction

Equatorial upwelling plays important roles in physical climate and marine ecosystems for time-mean and time-varying conditions. The equatorial upwelling induced by easterly winds creates cold sea surface temperatures in the eastern equatorial Pacific and Atlantic Oceans where the thermocline is shallow, and sharpens the zonal contrast of sea surface temperature (SST). This SST east–west contrast drives the Walker circulation because the zonal SST gradient maintains a zonal sea-level pressure gradient and consequent equatorial easterly wind, a lower branch of the Walker circulation (Bjerknes 1969). Additionally, variability in equatorial upwelling is a key aspect of the Bjerknes feedback, which plays an essential role in the El Niño–Southern Oscillation (ENSO) (e.g., Bjerknes 1969; Zebiak and Cane 1987; McPhaden 1999; Zhang et al. 2008; Fang and Wu 2008). In terms of the marine ecosystems, equatorial upwelling supplies nutrients including iron to the near-surface euphotic zone and supports the high biological productivity in the eastern equatorial Pacific, a high-nutrient and low-chlorophyll regions where primary production is limited by iron (Coale et al. 1996a,b; Martin et al. 1991). As such, future changes in physical climate and marine ecosystems due to global warming may be significantly influenced by the equatorial upwelling.

Change in equatorial upwelling under global warming has mainly been investigated by analyzing the outputs of climate models, in particular those in the World Climate Research Programme (WCRP) Coupled Model Intercomparison Project Phase 3 (CMIP3) multi-model dataset (Meehl et al. 2007). Vecchi and Soden (2007) analyzed outputs of

CMIP3 models for the Special Report on Emissions Scenarios (SRES) A1B scenario of the Intergovernmental Panel on Climate Change (IPCC). They found that upwelling of multi-model ensemble (MME) mean in the eastern equatorial Pacific reduces until the year 2100. By analyzing outputs of doubled CO¬2 emission experiments from CMIP3 models, Dinezio et al. (2009) consistently showed a reduction of MME mean vertical velocity at a depth of 50 m in the equatorial Pacific. In contrast, Seo and Xie (2011) found that upwelling will intensify in the eastern equatorial Atlantic until 2050 under the SRES-A1B scenario by conducting dynamical downscaling for a CMIP3 model.

Two major mechanisms for the future change in equatorial upwelling have been proposed: change in Ekman pumping near the surface and change in equatorial undercurrent (EUC) at depth. For the former, Dinezio et al. (2009) reported the weakening of MME mean Ekman divergence in the equatorial Pacific and an accompanying reduction in vertical velocity at a depth of 50 m. For the latter, Vecchi and Soden (2007) suggested that a flattening in the east–west thermocline slope induces a reduction in upwelling in the equatorial Pacific; the flatter thermocline's zonal slope is directly related to the reduction in upwelling, as the eastward-flowing EUC on eastward-shallowing pycnoclines generates upwelling. The EUC flattening is also accompanied by a basin-wide shoaling of the EUC, as reported by Luo and Rothstein (2011) and Sen Gupta et al. (2012) based on CMIP3 analyses. In addition to these two mechanisms, a nonlinear response of the equatorial zonal currents to the intensified cross-equatorial southerlies was suggested to enhance upwelling in the cold tongue of the equatorial Atlantic (Seo and Xie 2011).

Future changes in the Ekman pumping and those in the EUC, which are important aspects of changes in upwelling, are presumably caused by weakening of the trade wind.

Most climate models in the CMIP3 predict the slowdown of the Walker circulation under global warming (Vecchi and Soden 2007; Sen Gupta et al. 2012). The weaker trade winds in the future climate will cause a weakening of equatorial Ekman upwelling (Dinezio et al. 2009) and will also weaken upwelling associated with the EUC through a flatter thermocline (Vecchi and Soden 2007). The relation among the trade wind, upwelling and zonal thermocline gradient has been established for El Niño studies (e.g., Philander 1981; McPhaden 1993; Jin 1997; Kirtman 1997; McPhaden 1999; Wittenberg 2002; Zhang et al. 2008; Liu et al. 2017). Moreover, the tendency toward a weakening of the equatorial easterlies associated with the slowdown of the Walker circulation over the last 50 years has already been observed (Vecchi et al. 2006; Zhang et al. 2008). These results underline the importance of understanding how equatorial upwelling responds to the change in trade wind in a warmer climate.

Although previous studies have shown that future trade wind weakening will cause a reduction in equatorial upwelling, how the aforementioned two mechanisms contribute to the weakening of upwelling at different depths and different locations has not been systematically investigated. Therefore, the purpose of this study is to obtain a better understanding of the mechanisms of future changes in equatorial upwelling in the Pacific and Atlantic Oceans, where substantial reductions in upwelling are expected (Vecchi and Soden 2007). For this purpose, we systematically analyze output data from 24 CMIP5 models until 2100 under Representative Concentration Pathway (RCP) 8.5 by employing two analyses. One is to analyze the relation between MME mean and inter-model variability of future changes; this analysis can tell us how much of the change in MME mean can be explained by a specific change of a driver such as surface wind stress change. The other is to divide upwelling into isopycnal upwelling (the vertical component

of current velocity parallel to isopycnal surfaces) and diapycnal upwelling (the vertical component of current velocity perpendicular to isopycnal surfaces) (Bryden and Brady 1985; Sloyan et al. 2003). It can be expected that the change in isopycnal upwelling is strong where thermocline flattening is large, but in order to determine the relative contribution of isopycnal and diapycnal upwelling, a quantitative analysis is needed.

3.2. Data and Methods

The data used in this study are outputs of climate models participating in CMIP5 (Taylor et al. 2012), and were mainly obtained through the Program for Climate Model Diagnosis and Intercomparison (http://cmip-pcmdi.llnl.gov/cmip5/). We used the data for the historical experiment up to December 2005 and those for the high-emissions scenarios of RCP8.5 from January 2006 to December 2100. In this scenario, greenhouse gas concentration and thus radiative forcing do not stabilize by 2100 (Liddicoat et al. 2013). We used outputs of 24 models, as listed in Table 1, and analyzed only the first ensemble of each model so as to treat all models equally.

Zonal and meridional components of velocity from CMIP5 outputs were estimated by a coordinate rotation using original velocity components in the directions of the model coordinate and coordinate angles relative to the meridian estimated from the coordinates. All model outputs were interpolated to a common horizontal grid with 1° × 1° resolution, and the three-dimensional data were further interpolated to a common set of 28 vertical levels with 13 levels in the top 400 m of the ocean.

In order to understand the mechanisms of change in MME mean, we used two analyses. The first was an analysis of the relation between MME mean and inter-model variability. It is useful to illustrate here how this analysis works. Figure 3.1 shows a schematic scatter plot of epoch differences, denoted by Δ, of explanatory variable X and

response variable Y among models. The dots indicate respective model changes and the plus symbol (+) denotes the change in MME mean. In the case where the change in MME mean is on the regression line, the change in MME mean of ΔY can be estimated from the regression relation, namely, $a\,\Delta X_{MME} + b$, where a is the regression slope and b is the intercept. The first term is the change in MME mean for ΔY that is explained by the change for ΔX, while the intercept is unrelated to the change of explanatory variable. Therefore, a ratio given by $a\,\Delta X_{MME}/\Delta Y_{MME}$ represents how much of the change in MME mean of Y can be explained by that of X.

The second analysis is the division of total upwelling (w_t) into isopycnal upwelling (w_i) and diapycnal upwelling (w_d), following Pedlosky (1996). Since an isopycnal upwelling is a vertical velocity component derived from isopycnal flow, one can obtain isopycnal upwelling from the following advection equation:

$$w_i \equiv u\frac{\partial h}{\partial x} + v\frac{\partial h}{\partial y} \qquad (3.1)$$

where h is the depth of isopycnals (positive upward), u and v are the zonal and meridional velocities, respectively, and w_i is the isopycnal upwelling velocity. The diapycnal upwelling is calculated as the difference between the total upwelling and the isopycnal upwelling, that is,

$$w_d = w_t - w_i \qquad (3.2)$$

where w_t and w_d are the total and diapycnal upwelling velocities, respectively. The concepts of isopycnal and diapycnal upwelling have been introduced by previous studies of equatorial circulations and the Pacific cold tongue (Bryden and Brady 1985; Sloyan et al. 2003), but to the authors' knowledge they have not previously been employed in studies of future upwelling changes.

3.3. Results

3.3.1. Relation between upwelling and driver changes

From 1971–2000 to 2071–2100, the MME mean upwelling decreases in the equatorial Pacific and Atlantic at a depth of about 0–200 m and increases in the eastern Indian Ocean at a depth of about 0–100 m (Fig. 3.2). The equatorial Pacific has the largest upwelling decrease among the tropical oceans. The Pacific upwelling decreases most strongly around 120°W at a depth of 100 m, by about 30% of its climatology, and this vertical velocity change is three times larger than that in the Atlantic. The MME mean upwelling strongly decreases in the eastern Pacific basin at a depth of 250 m or shallower, where all models agree on the sign of the change, and the amplitude of the upwelling change is statistically significant according to a Wilcoxon signed-rank test at a 5% significance level (stippled regions in Fig. 3.2). At depths between 50 and 75 m, a relatively strong reduction in MME mean upwelling appears in the central Pacific, but only 70% of the models agree on the sign of the change. In the western Atlantic, 22 of the 24 models show a reduction in upwelling at depths of 25–150 m. At deeper depths than 150 m, the MME mean upwelling changes only a little. In the Indian Ocean, changes in upwelling are generally insignificant. These results are consistent with those of Vecchi and Soden (2007), who analyzed the outputs of CMIP3 models.

We first estimate how much of the inter-model variability in upwelling change can be explained by wind stress and stratification changes for the Pacific Ocean. Here, we also examined the influence of stratification change (Fig. 3.3b) because increased stratification has weakened upwelling in the current climate (e.g., Fiedler 2002). Figure 3.3a shows the inter-model correlation between epoch differences of equatorial upwelling

and those of zonally averaged zonal wind stress over the eastern Pacific, and indicates that the upwelling change in the eastern equatorial Pacific is significantly correlated with wind stress change in that region. Therefore, we suggest that the inter-model variability in upwelling reduction around the EUC core and at shallower depths in the eastern equatorial Pacific is mainly induced by local weakening of the trade wind over the eastern Pacific basin. Near the sea surface in the central Pacific (where, as mentioned above, the models disagree on the sign of the upwelling change), the inter-model variability in the upwelling change is significantly correlated with the zonally averaged wind stress change across the entire Pacific basin (not shown). This indicates that the inter-model variability in upwelling change near the sea surface in the central Pacific is well explained by the inter-model variability in the trade wind change averaged over the entire basin. The correlations between the changes in upwelling and changes in stratification are significant in some regions (Fig. 3.3b), but do not substantially overlap with the strong changes in upwelling.

In order to understand whether the mechanism of the inter-model variability of changes in upwelling can also explain changes in MME mean, we plotted scatter diagrams between the change in zonal wind stress and response of each model. Figure 3.4a shows the relation between eastern basin-averaged upwelling change near the surface and eastern basin-averaged zonal wind stress. The local wind stress change well explains the inter-model variability in upwelling change near the sea surface in the eastern Pacific, with a correlation of −0.50, consistent with the strong negative correlation near the surface shown in Fig. 3.3a. The MME mean, denoted by a plus symbol (+), is located on the regression line. The ratio of $a\,\Delta X_{\mathrm{MME}}$ to ΔY_{MME}, which gives a measure of how much of the change in MME mean is explained by the inter-model

regression relation, as illustrated in Fig. 3.1, is 55%, where ΔX_{MME} and ΔY_{MME} are the changes in MME mean in the zonal wind stress and near-surface upwelling, respectively. Thus, about half of the upwelling reduction near the surface is explained by the weakened trade wind over the eastern Pacific basin. Around the EUC core in the eastern Pacific, the models that show a strong reduction in upwelling exhibit strong weakening of the local trade wind ($r = -0.72$) (Fig. 3.4b), consistent with the previous result shown in Fig. 3.3a. The MME mean is again located on the regression line, and the ratio $a\,\Delta X_{MME}/\Delta Y_{MME}$ is 46%. This means that about half of the MME mean upwelling reduction around the EUC core is explained by the weakened local trade wind. Consequently, locally weakened trade wind due to global warming explains not only the inter-model variability but also changes in MME mean for a weakening of near-surface upwelling and a reduction of subsurface maximal upwelling at depths of 75–200 m in the eastern equatorial Pacific.

In the western Atlantic, both a weakened trade wind and enhanced stratification are significantly correlated with a reduction in upwelling at depths of 50–150 m (Figs. 3.5a,b), with the negative correlations covering the region of strong upwelling reduction. The area-averaged upwelling change at depths between 25 and 100 m in the western Atlantic is highly correlated across models with the basin average of change in equatorial zonal wind ($r = -0.81$) and also with the basin average of change in stratification ($r = -0.70$) (Fig. 3.6). However, the changes in zonal wind stress and the enhanced stratifications are strongly correlated in the Atlantic ($r = 0.60$), in contrast to the quite small correlation in the Pacific ($r = 0.11$). This dependency between the change in trade wind and the change in stratification makes it difficult to distinguish the relative contributions of the two to the reduction in upwelling in the Atlantic.

The covariation of the zonal wind stress and stratification also causes difficulty when interpreting the causes of change in MME mean. Although the ratio of $a\,\Delta X_{MME}/\Delta Y_{MME}$ between the change in upwelling and change in stratification (150%) is larger than that between the change in upwelling and change in zonal wind stress (63%), the dependency does not allow one to conclude that the former is more important than the latter.

3.3.2. Changes in isopycnal and diapycnal upwelling

In order to obtain a better physical explanation for the change in upwelling, we divided upwelling into isopycnal and diapycnal upwelling, as explained in section 3.2. Hereafter, upwelling without such division is referred to as total upwelling. The change in total upwelling shown in Fig. 3.2 is given by the sum of the isopycnal upwelling (Figs. 3.7a,c) and diapycnal upwelling (Figs. 3.7b,d). The statistically significant change in isopycnal upwelling occurs at depths between 75 and 200 m in the eastern Pacific (Fig. 3.7a), where isopycnals are strongly tilted, as will be shown later, whereas significant diapycnal change occurs at depths between 0 and 75 m in the central to eastern Pacific (Fig. 3.7b). In the equatorial Atlantic, isopycnal and diapycnal upwelling show very little significant change, due to the small amplitude of changes in MME mean relative to large inter-model variability (Figs. 3.7c,d). We will therefore focus our attention on the upwelling change processes in the equatorial Pacific, especially the eastern equatorial Pacific, where upwelling significantly decreases. Next, we examine how near-surface diapycnal upwelling and isopycnal upwelling at deeper levels are related to changes in subsurface density and circulation.

The near-surface upwelling in the eastern Pacific is closely related to the Ekman pumping. In the current climate, the mean poleward flow at depths of 0–50 m indicates the Ekman divergence (see contours in Fig. 3.8b). Zonally averaged meridional velocities

weaken in this depth range, especially around 5°S and 5°N, except at the surface (Fig. 3.8b), indicating the reduction of the Ekman divergence along the equator. Because vertically integrated Ekman transport solely depends on the wind stress across the same latitudes, the change in Ekman divergence should be due to the change in zonal wind stress. This is consistent with the aforementioned strong correlation between the change in total upwelling and the change in zonal wind stress (Fig. 3.3a). Consequently, the weakening of the near-surface total upwelling in the eastern Pacific, due to the diapycnal upwelling reduction, is closely related to the reduction of the Ekman divergence caused by the weakened trade wind.

The reduction in isopycnal upwelling, which dominates the changes in total upwelling between 75–200 m in the eastern Pacific, should be linked to the zonal velocity reduction and/or zonal isopycnal flattening. The zonal velocity significantly reduces beneath the EUC core in the current climate, accompanied by zonal velocity enhancement above the core (Fig. 3.8a), suggesting an upward migration of the EUC. Shallowing of the EUC due to global warming was reported by Luo et al. (2015) and Sen Gupta et al. (2012), but these studies did not investigate the relation between the EUC and upwelling. For the other mechanism, namely, isopycnal flattening, the isopycnals corresponding to the EUC core indicate a flatter zonal slope in the future than at present (Fig. 3.8c). Therefore, both zonal velocity reduction and zonal isopycnal flattening can contribute to reduced isopycnal upwelling in the eastern equatorial Pacific. We quantitatively estimate respective contributions below.

The contributions of zonal velocity change and isopycnal slope change to the reduction of MME mean isopycnal upwelling at depths between 75 and 200 m can be calculated from a linear expansion of the advection equation (Eq. 3.1). We separate each

dependent variable into mean and difference parts as follows:

$$\Delta w_i \approx \Delta u\left(\overline{\frac{\partial h}{\partial x}}\right) + \bar{u}\Delta\left(\frac{\partial h}{\partial x}\right) + \Delta v\left(\overline{\frac{\partial h}{\partial y}}\right) + \bar{v}\Delta\left(\frac{\partial h}{\partial y}\right) \qquad (3.3)$$

where Δ indicates the difference between the two epochs (2071–2100 minus 1971–2000), and overbar ($\bar{}$) indicates the mean value for the period 1971–2000. The third and fourth terms can be ignored because these two terms are much smaller than the first and the second terms. The first (second) term indicates the change in isopycnal upwelling associated with only zonal velocity (zonal isopycnal gradient) change. Figures 3.9a and 3.9b show the first and second terms of Eq. (3.3), respectively. A visual inspection of these figures and Fig. 3.7a clearly indicates that the change in isopycnal upwelling at depths between 75 and 200 m in the eastern equatorial Pacific, as shown in Fig. 3.7a, is due to the change in zonal isopycnal gradient. This indicates that the weakening of MME mean isopycnal upwelling in the eastern Pacific is mainly induced by a zonal flattening of the east–west slope of the EUC.

Additionally, the changes in upwelling due to the flattening of the EUC slope dominantly explain the inter-model variability of changes in isopycnal upwelling with the regression slope of 0.71 in the eastern Pacific (Fig. 3.9c). This regression slope is 1.5 times larger than the slope of 0.47 for changes in upwelling due to the zonal velocity change. Consequently, flattening of the zonal pycnocline slope plays a dominant role in the inter-model variability of change in isopycnal upwelling as well as the change in MME mean at depths between 75 and 200 m in the eastern Pacific.

Because it is widely known that the zonal gradient of the equatorial pycnocline is well explained by a reduced gravity model (e.g., Jin 1997), it is interesting to ask a further question: how can the EUC flattening be explained quantitatively by a reduced gravity model? To address this question, we employ a linearized reduced gravity model

for the change in isopycnal gradient, which can be expressed by the changes in stratification and zonal wind stress:

$$\Delta\frac{dh}{dx}=\frac{1}{\rho_0 H}\Delta\left(\frac{\langle\tau^x\rangle}{g'}\right)\approx\frac{1}{\rho_0 H}\frac{1}{\overline{g'}}\Delta\langle\tau_x\rangle+\frac{1}{\rho_0 H}\overline{\langle\tau_x\rangle}\Delta\frac{1}{g'} \qquad (3.4)$$

where $\langle\tau^x\rangle$ is the zonally averaged zonal wind stress along the equator, g' is the reduced gravity, ρ_0 is the reference density, h is the total local depth of the pycnocline, and H is the constant background layer thickness. The first term of the right-hand side indicates the influence of the change in zonal wind stress, while the second term indicates the changes in the density difference between the surface layer and deeper layer. We employ this model in the eastern equatorial Pacific (140°W–100°W), where change in isopycnal gradient plays the dominant role in the change in isopycnal upwelling (Fig. 3.9b). The reference density and the layer thickness are set to 1025 kg/m^3 and 75 m, respectively. Reduced gravity is calculated using the zonal mean (140°W–100°W) density between the surface and the pycnocline and that between the pycnocline and a depth of 1000 m, where pycnocline is the depth of the isopycnal (h).

In order to know whether the reduced gravity model can be applied to EUC flattening, we examine the relationship between $\Delta dh/dx$ and $\Delta\langle\tau_x\rangle$ for the first term of Eq. (3.4) and that between $\Delta dh/dx$ and $\Delta\,1/g'$ for the second term. Here, the isopycnal depth (h) is defined as a contour of area-averaged density in 140°W–100°W at a depth of 75 m along the equator. The correlation for the first term is as high as 0.84, but that for the second term is very low (r = 0.17). Thus, only the first term, i.e., the changes in wind stress, plays an important role in the slope change of the thermocline. The regression slope for the first term is close to that which is expected from the reduced gravity model; that is, the regression slope is larger by only 25% than the coefficient of the first term, $1/(\rho_0 H\overline{g'})$, with the regression line almost crossing the origin. These results indicate that

the EUC flattening is explained by the change in zonal wind stress, which is consistent with the reduced gravity model.

3.4. Summary and Discussion

We investigated the change in equatorial upwelling and its mechanisms in the Pacific and Atlantic Oceans until 2100 under RCP8.5 by analyzing MME mean along with differences among models using outputs from 24 CMIP5 models. Zonal and meridional components of current velocities were estimated from velocities in the original coordinate system by a coordinate rotation, and three-dimensional velocity components of CMIP5 multi-models were used for the first time in an upwelling study, to the authors' knowledge. The estimation of zonal and meridional velocities allowed us to investigate three-dimensional circulation change and to diagnose isopycnal and diapycnal upwelling.

In the eastern equatorial Pacific, the MME mean and inter-model variability in the changes in total upwelling is explained by two mechanisms. One is the decrease in diapycnal upwelling near the surface (Fig. 3.7b) that is associated with the weakened Ekman divergence (Fig. 3.8b) due to locally weakened trade wind over the eastern Pacific basin (Figs. 3.3a and 3.4a). The other is the decrease in isopycnal upwelling at depths of 75–200 m around the EUC core (Fig. 3.7a). This decrease is induced by EUC flattening (Fig. 3.9) due to locally weakened trade wind over the eastern Pacific basin (Figs. 3.3a and 3.4b). These mechanisms of upwelling changes are at work for both the MME mean and inter-model variability. The major features and mechanisms of upwelling reduction in the equatorial Pacific between the years 2000 and 2100 are summarized in Fig. 3.10.

In the equatorial Atlantic, the inter-model variability in the reduction in total upwelling at a depth of 25–150 m, where there is a local maximum of reduction in MME mean upwelling, is significantly related to both the weakened trade wind and enhanced

stratification (Fig. 3.5). Both these drivers also explain the change in MME mean upwelling at depths of 25–150 m (Fig. 3.6). However, how much of the total upwelling changes of MME mean and inter-model variability are contributed by each driver is unclear since the changes in wind and stratification are not independent in the equatorial Atlantic. Very little significant change in isopycnal and diapycnal upwelling is projected due to the small amplitude of changes in MME mean relative to the large inter-model variability (Figs. 3.7c,d). The mechanisms of upwelling change in the equatorial Atlantic are not well identified by the present analyses.

The reduction in near-surface diapycnal upwelling in the eastern equatorial Pacific can impact the SST there. The response of equatorial SST to global warming attracts much attention because the change in equatorial SST is quite important for tropical climate conditions such as ENSO (e.g., Knutson and Manabe 1995; Meehl and Washington 1996; Liu 1998; Meehl et al. 2000; Zhang et al. 2008; Dinezio et al. 2009; Liu et al. 2017). In particular, it is suggested that stronger warming in the eastern equatorial Pacific than in the surrounding regions leads to more frequent extreme or strong eastern Pacific El Niños (Cai et al. 2014, 2018). A possible mechanism for this future change in SST in the equatorial Pacific is reduced upwelling in response to weaker trade wind (Zhang et al. 2008; Dinezio et al. 2009). Dinezio et al. (2009) suggested that the upwelling reduction at a depth of 75 m increases the SST in the eastern equatorial Pacific. Our results indicate that upwelling reduction at this depth is closely related to the local wind (Fig. 3.3a) and is mainly due to diapycnal upwelling (Fig. 3.7b), which contributes 88% of equatorial upwelling between 140°W–100°W. This suggests that changes in the local Ekman divergences rather than the basin-scale circulation change including EUC are important in SST change. Therefore, our results are useful for a deeper understanding

the SST change due to global warming in the eastern equatorial Pacific.

The reduction in total upwelling in the equatorial Pacific can impact the future marine primary production. In particular, the reduction of total upwelling to the euphotic zone can significantly alter primary production because nutrients including iron are the limiting factor of photosynthesis. The upwelling region in the eastern equatorial Pacific is a high-nutrient and low-chlorophyll region due to the limited iron supply (e.g., Martin et al. 1991). The EUC plays an important role in the supply of iron to this region (e.g., Christian et al. 2002; Coale et al. 1996a; Gorgues et al. 2010; Mackey et al. 2002; Ryan et al. 2006; Slemons et al. 2010). Bopp et al. (2013) showed a robust reduction in the export production of organic particles at a depth of 100 m—which is a measure of the biological production in the upper 100 m—in the eastern equatorial Pacific in the 21st century among CMIP5 models. This reduction is probably related to the reduced nutrient supply to the euphotic layer associated with the weakened upwelling in this region. At a depth of 100 m, the changes in upwelling are dominated by isopycnal upwelling (Figs. 3.7a,b). Therefore, changes in isopycnal upwelling may play an important role in marine ecosystems.

Table 3.1. CMIP5 models used in this study.

	Model	Institution	OGCM resolution (lon grid points × lat grid points × levels)
A	BCC-CSM1-1	Beijing Climate Center, China Meteorological Administration, China	360 × 232 × 40
B	CanESM2	Canadian Centre for Climate Modelling and Analysis, Canada	256 × 192 × 40
C	CCSM4	National Center for Atmospheric Research (NCAR), United States	320 × 384 × 60
D	CESM1-BGC		
E	CMCC-CESM	Centro Euro-Mediterraneo per i Cambiamenti Climatici, Italy	182 × 149 × 31
F	CMCC-CM		
G	CMCC-CMS		
H	CNRM-CM5	Centre National de Recherches Mété orologiques, France	362 × 292 × 42
I	CSIRO-Mk3-6-0	CSIRO and Queensland Climate Change Centre of Excellence, Australia	192 × 189 × 31
J	FGOARS-s2	LASG, Institute of Atmospheric Physics, Chinese Academy of Sciences	360 × 196 × 30
K	GFDL-CM3	NOAA/Geophysical Fluid Dynamics Laboratory, United States	360 × 200 × 50
L	GFDL-ESM2M		360 × 200 × 50
M	GISS-E2-R	NASA Goddaard Isntitute for Space Studies, United States	288 × 180 × 32
N	HadGEM2-CC	Met Office Hadley Centre, United Kingdom	360 × 216 × 40
O	HadGEM2-ES		
P	IPSL-CM5A-LR	Institute Pierre-Simon Laplace, France	182 × 149 × 31
Q	IPSL-CM5A-MR		
R	IPSL-CM5B-LR		
S	MPI-ESM-LR	Max Planck Institute for Meteorology, Germany	256 × 220 × 40
T	MPI-ESM-MR		802 × 404 × 40
U	MRI-CGCM3	Meteorological Research Institute, Japan	360 × 368 × 51
V	MRI-ESM1		
W	NorESM1-M	Norwegian Climate Centre, Norway	320 × 384 × 70
X	NorESM1-ME		

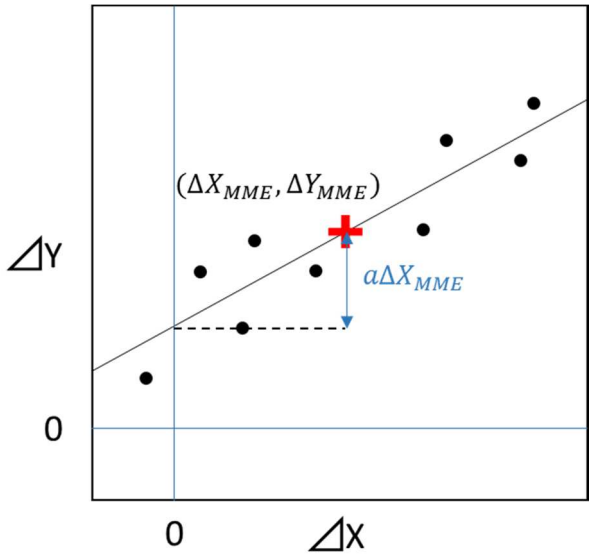

Figure 3.1. Schematic scatter diagram between epoch differences of explained variable X and response variable Y among climate models. The dots indicate respective model changes, and the plus symbol (+) denotes the MME mean change. The ΔX_{MME}, ΔY_{MME}, and a represent the MME mean changes in X and Y, and the regression slope, respectively. The black line indicates the regression line. The blue arrow indicates the ΔY_{MME} associated with ΔX_{MME}. The dashed line indicates ΔY at which regression line crosses the line of zero ΔX.

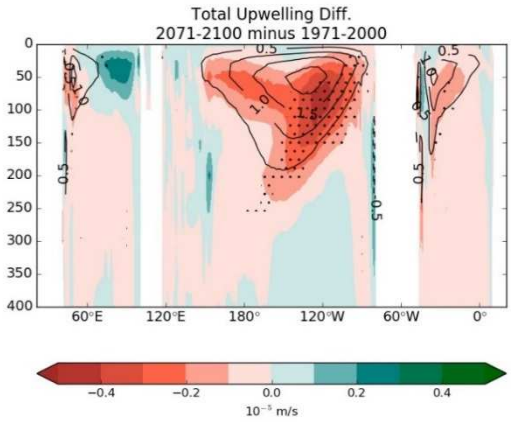

Figure 3.2. Total differences in upwelling along the equator (color) between 1971–2000 and 2071–2100 for 24-model MME mean under RCP8.5. Contours indicate the mean total upwelling for the period 1971–2000. Stippling indicates regions where projected changes are statistically significant according to a Wilcoxon signed-rank test with a 5% significance level and more than 90% of the models agree on the sign of the change.

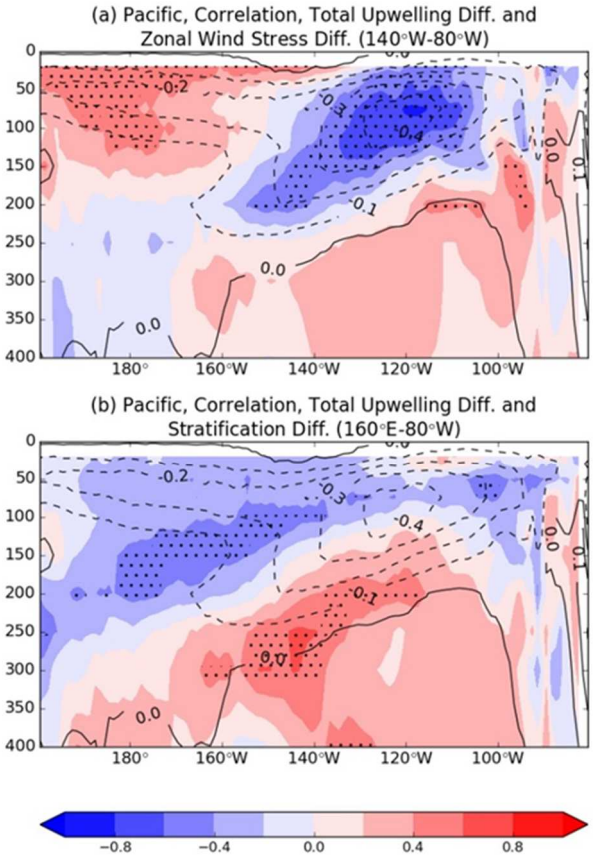

Figure 3.3. Inter-model correlation coefficient (color) between epoch differences in total upwelling at the equator and: (a) epoch differences in eastern Pacific basin-averaged zonal wind stress (140°W–80°W along the equator), and (b) epoch differences in the basin-averaged stratification (160°E–80°W along the equator between surface and 100 m). The epochs are 1971–2000 and 2071–2100 under RCP8.5. Contours indicate epoch differences in upwelling in all panels.

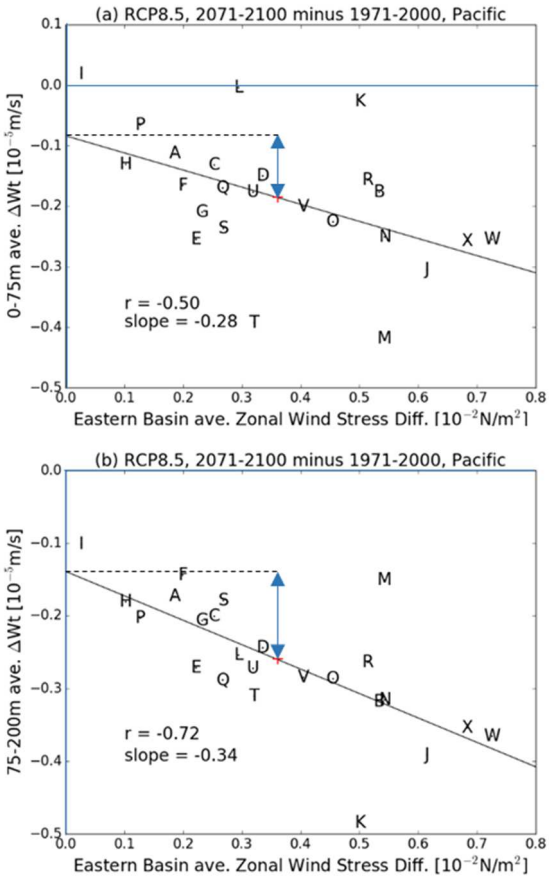

Figure 3.4. (a) Scatter diagram of epoch differences of area-averaged upwelling (140°W–100°W at depths of 0–75 m along the equator) and eastern Pacific basin-averaged zonal wind stress (140°W–80°W) among climate models. The epochs are 1971–2000 and 2071–2100 under RCP8.5. The plus symbol (+) denote the MME, and letters denote the respective models (Table 1). The black line indicates the regression line. The blue arrow indicates the change in MME mean upwelling associated with the MME mean basin-averaged zonal wind stress change. The dashed line indicates the change in MME mean upwelling at the point where the regression line crosses the line of zero zonal wind stress change. Correlation coefficient and slope are shown in the panels. (b) Same as (a), but for area-averaged upwelling (140°W–100°W at depths of 75–200 m along the equator) and eastern basin-averaged zonal wind stress (140°W–80°W).

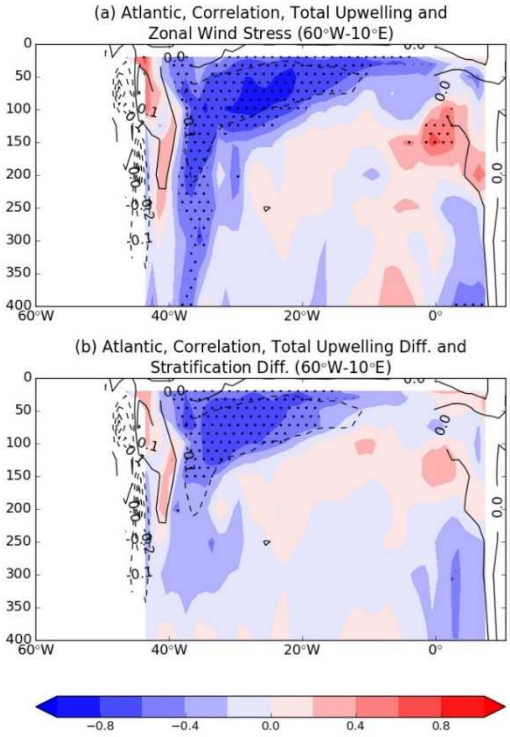

Figure 3.5. Same as Fig. 3.3a and 3.3c, but for the Atlantic. The averaged area of change in zonal wind stress and change in stratification is 60°W–10°E along the equator.

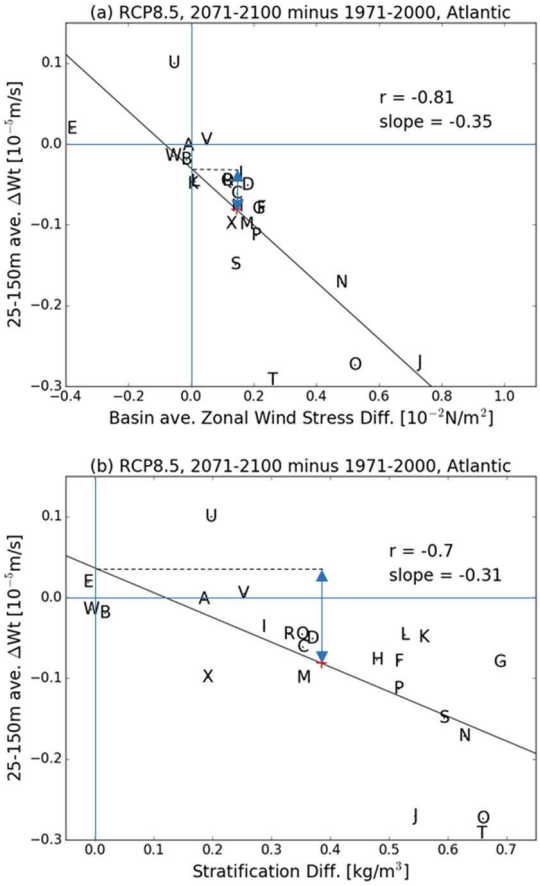

Figure 3.6. (a) Same as Fig. 3.4a, but for area-averaged total upwelling in the Atlantic (40°W–20°W at depths of 25–150 m along the equator) and Atlantic basin-averaged zonal wind stress (60°W–10°E). (b) Same as (a), but for area-averaged upwelling (40°W–20°W at 25–150 m depth along the equator) and basin-averaged stratification (60°W–10°E along the equator between the surface and a depth of 100 m).

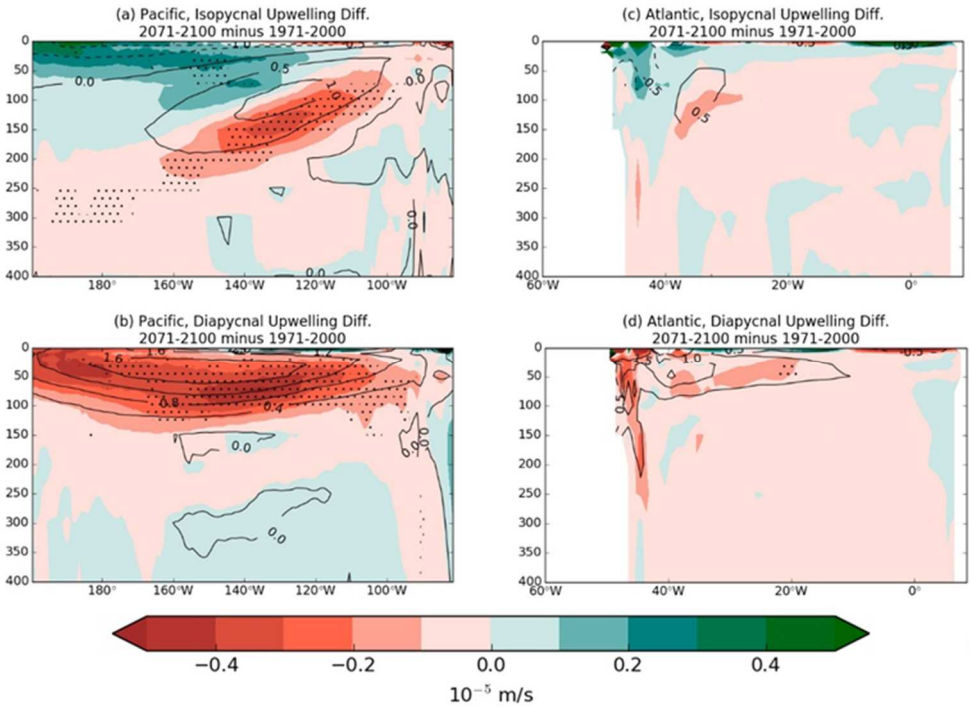

Figure 3.7. Differences in isopycnal upwelling (color) between 1971–2000 and 2071–2100 for 24-model MME under RCP8.5 (a) in the equatorial Pacific and (c) in the equatorial Atlantic. Contours indicate mean isopycnal upwelling for the period 1971–2000. Stippling indicates regions where projected changes are statistically significant according to a Wilcoxon signed-rank test with a 5% significance level and more than 90% of the models agree on the sign of the change. Panels (b) and (d) are the same as (a) and (c), respectively, but for differences in diapycnal upwelling.

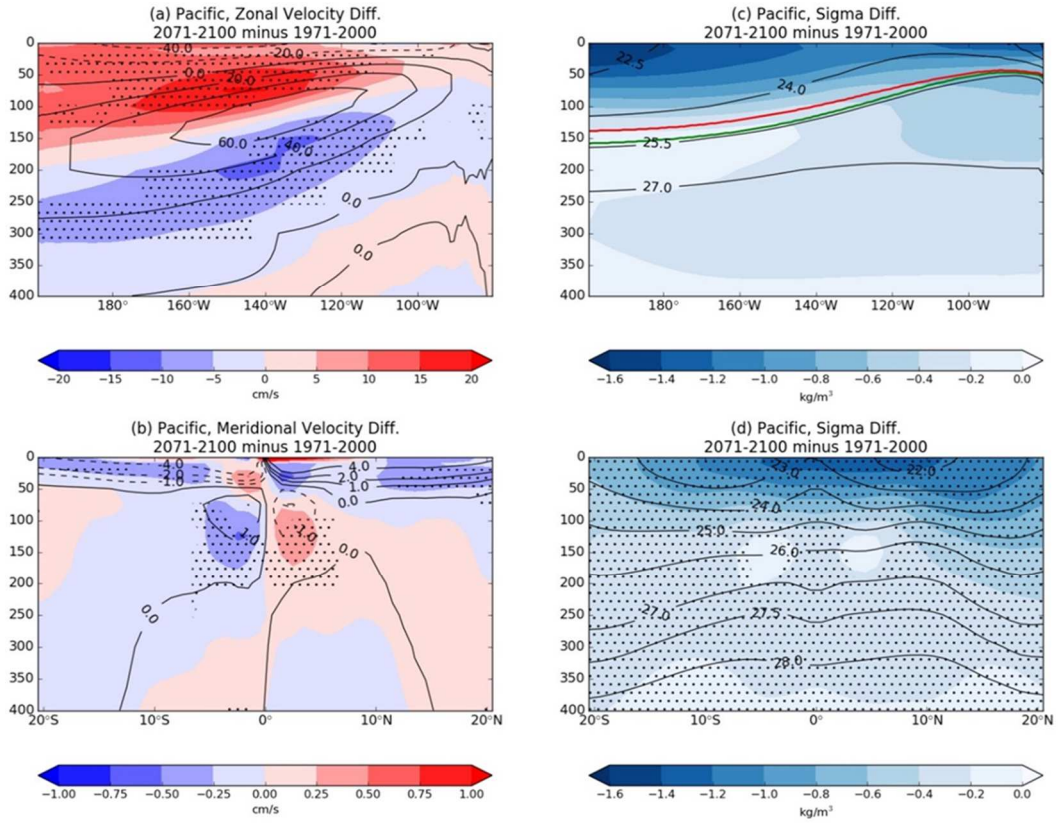

Figure 3.8. Depth-longitude cross-sections along the equator of (a) zonal velocity difference and (c) σ difference between 1971–2000 and 2071–2100 for 24-model MME under RCP8.5 (color). Contours indicate the mean (a) zonal velocity and (c) σ for the periods 1971–2000. Panels (b) and (d) are the basin-averaged depth–latitude cross-sections (160°E–80°W) of (b) meridional velocity and (d) σ. Contours indicate the mean (b) meridional velocity and (d) σ for the period 1971–2000. Stippling indicates regions where projected changes are statistically significant according to a Wilcoxon signed-rank test with a 5% significance level and more than 90% of the models agree on the sign of the change. Green and red lines in (c) indicate the isopycnals of averaged σ along the EUC core (zonal velocity maxima) over the entire Pacific basin for the periods 1971–2000 and 2071–2100, respectively.

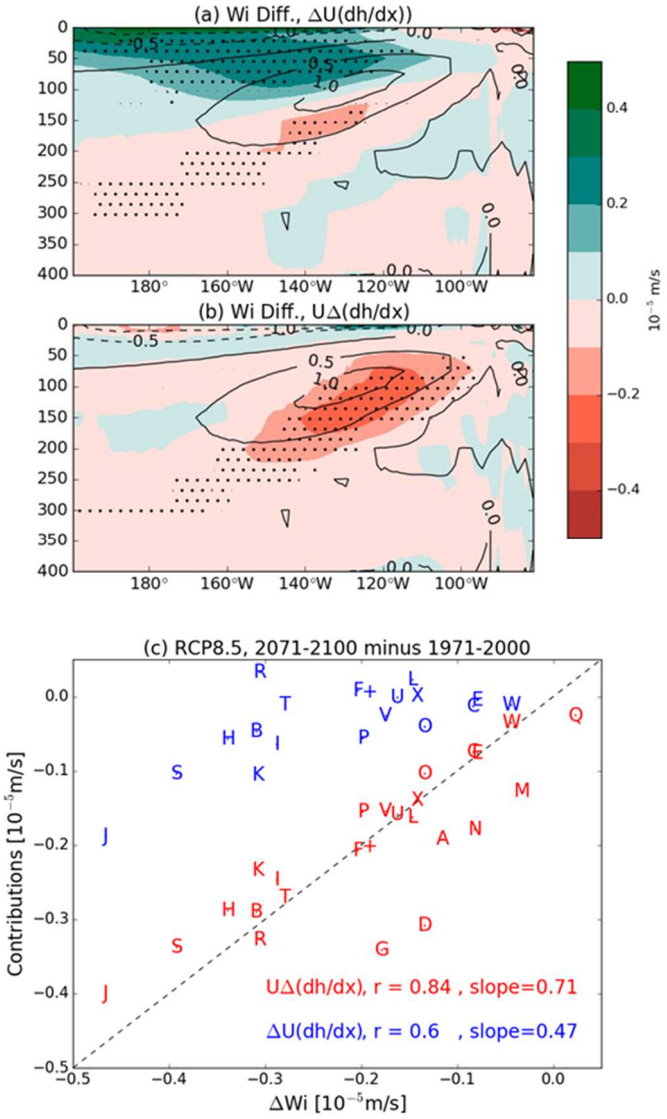

Figure 3.9. (a) Changes in isopycnal upwelling due to differences in zonal velocity along the equator between 1971–2000 and 2071–2100 for 24-model MME under RCP8.5 (color). (b) Same as (a), but isopycnal upwelling changes due to differences in zonal isopycnal gradient. Contours indicate the mean zonal component of isopycnal upwelling for the period 1971–2000 in all panels. (c) Scatter diagram of epoch differences of area-averaged isopycnal upwelling (140°W–100°W at a depth of 100 m along the equator) and contributions of zonal velocity (blue) and zonal isopycnal gradients (red) among climate models. The epochs are 1971–2000 and 2071–2100 under RCP8.5. The plus symbol (+) denotes the MME and letters denote the respective models (Table 1). Correlation coefficients and slopes are shown in the panel.

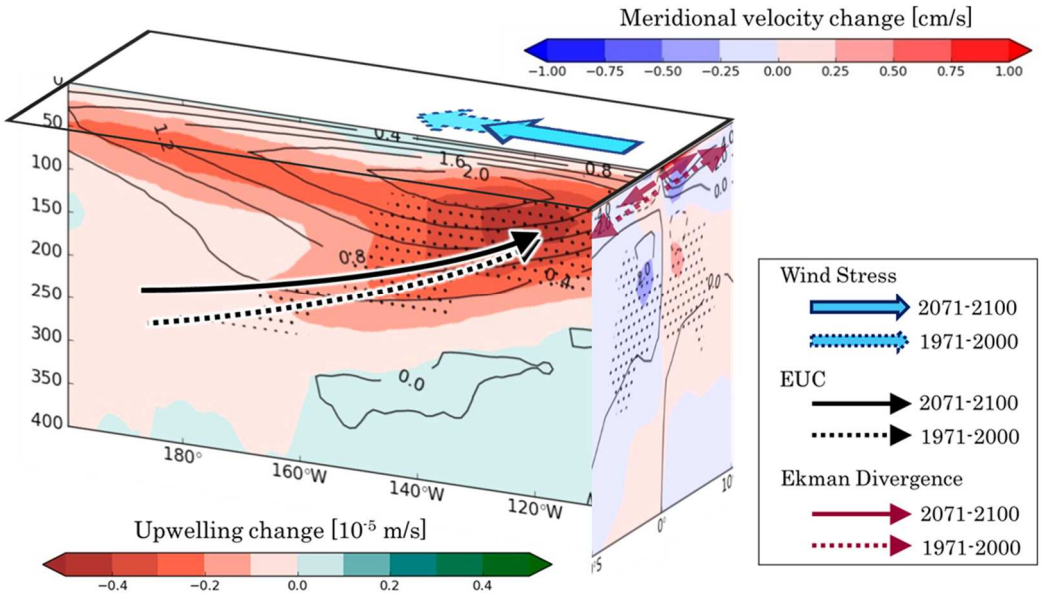

Figure 3.10. Schematic diagram illustrating the mechanisms of upwelling reduction in the eastern equatorial Pacific from 1971–2000 to 2071–2100. The weakening of trade winds (blue arrows) in the eastern Pacific induces weakening of the Ekman divergence leading to the reduced diapycnal upwelling near the surface, and also causes the EUC flattening and resultant reduction in isopycnal upwelling at depths of 75–200 m. The variables shown in the zonal cross-section are the same as in Fig. 3.2, and those in the meridional cross-section are the same as in Fig. 3.8b.

Chapter 4

General Summary

The mechanisms of two aspects of the ocean responses to the global warming, i.e., the sea level rise in the North Pacific and upwelling change along the equator, are examined in terms of three-dimensional subsurface structure changes in this study. We used outputs from CMIP5 models and analyzed the MME mean along with differences among models. In this chapter, we summarize the major findings of chapters 2 and 3.

In chapter 2, the sea level rise in the North Pacific is investigated. The DSL, which is defined as sea level deviation from the global mean sea level of climate models, will rise in the western North Pacific around the KE, consistent with previous studies (Yin et al. 2010; Yin 2012; Sueyoshi and Yasuda 2012; Zhang et al. 2014; Church et al. 2013; Slangen et al. 2014). Subsurface density analysis indicates that DSL rise around the KE is associated with a density decrease of STMW and also with a northward KE migration. The former is more effective between 2000 and 2100 for both RCP4.5 and RCP8.5 and the latter is more effective between 2100 and 2300 for RCP8.5. The STMW density decrease is related to a large heat uptake to the south and southeast of Japan, while the northward KE migration is associated with the poleward shift of the wind stress field. These features are commonly found in MME means and the relations among representative quantities produced by different climate models.

In chapter 3, upwelling changes along the equator are investigated. The equatorial upwelling will decrease in the Pacific and Atlantic at about 0-200 m depths until 2100. In the eastern equatorial Pacific, both of the MME mean and inter-model variability in the upwelling change is explained by following two mechanisms: (1) the upwelling decrease near the surface associated with the weakened Ekman divergence

due to weakened trade wind; (2) the upwelling decrease at 75-200 m depths induced by the EUC flattening due to locally weakened trade wind over the eastern basin. In the equatorial Atlantic, both of the MME mean and inter-model variability in the upwelling change is explained by the changes in the trade wind and stratification. These drivers, i.e., wind and stratification, however, are not independent in the equatorial Atlantic, and therefore how much of the upwelling changes of MME mean and inter-model variability are contributed by each driver is still unclear. Although upwelling change in the Atlantic is weaker than that in the Pacific, the future study is needed to clarify the mechanism of upwelling change in the equatorial Atlantic.

These findings owe two common approaches we employed in this thesis. One is to analyze inter-model variability of future changes. This analysis told us the origin of model uncertainties, and often gave us the plausible mechanism for MME mean change. The other one is to analyze three-dimensional oceanic changes including circulations and water mass formations. This analysis of subsurface oceanic response improved understanding of the future DSL and equatorial upwelling change, i.e. a lager contribution of heat uptake of STMW for the DSL rise until 2100 in the western North Pacific and a specific contribution of the EUC flattening to the upwelling decrease at 75-200 m depths in the eastern equatorial Pacific, in this thesis. Therefore, in order to better understand the oceanic responses to global warming, it is important to evaluate the changes in three-dimensional structure of subsurface ocean.

Acknowledgement

I would like to express my most sincere gratitude to my academic supervisor Prof. Shoshiro Minobe for his many valuable suggestions and discussion throughout the study. Without his support and encouragement, I could not complete my PhD study. I would also like to thank my PhD committee, Profs. Masaru Inatsu, Yoshinori Sasaki, and Fumio Mitsudera for fruitful discussions. Finally, I wish to express my thanks to my parents, Hideki Terada and Toshiko Terada for supporting me to pursue the PhD degree.

References

Bjerknes, J. (1969), Atmospheric teleconnections from equatorial Pacific, Mon. Wea. Rev., 97, 163-172.

Boer, G. J. (2009), Changes in interannual variability and decadal potential predictability under global warming, J. Clim., 22, 3098-3109.

Bopp, L., Resplandy, L. Orr, J. C. Doney, S. C. Dunne, J. P. Gehlen, M. Halloran, P. Heinze, C. Ilyina, T. Seferian, R. Tjiputra, J. Vichi, M. (2013), Multiple stressors of ocean ecosystems in the 21st century: projections with CMIP5 models, Biogeosciences, 10, 6225-6245, doi:10.5194/bg-10-6225-2013.

Bryden, H. L., and E. C. Brady (1985), Diagnostic model of the 3-dimensional circulation in the upper equatorial Pacific-Ocean, J. Phys. Oceanogr., 15, 1255-1273.

Cai, W. J., Borlace, S. Lengaigne, M. van Rensch, P. Collins, M. Vecchi, G. Timmermann, A. Santoso, A. McPhaden, M. J. Wu, L. X. England, M. H. Wang, G. J. Guilyardi, E. Jin, F. F. (2014), Increasing frequency of extreme El Niño events due to greenhouse warming, Nat. Clim. Change, 4, 111-116, doi: 10.1038/NCLIMATE2100.

Cai, W. J., G. J. Wang, B. Dewitte, L. X. Wu, A. Santoso, K. Takahashi, Y. Yang, A. Carreric, and M. J. McPhaden (2018) Increased variability of eastern Pacific El Nino under greenhouse warming, Nature, 564, 201-206, doi: 10.1038/s41586-018-0776-9.

Chen, L., T. Li, and Y. Q. Yu (2015), Causes of strengthening and weakening of ENSO amplitude under global warming in four CMIP5 models, J. Clim., 28, 3250-3274.

Cheon, W. G., Y.-G. Park, S.-W. Yeh, and B.-M. Kim (2012), Atmospheric impact on the northwestern Pacific under a global warming scenario, Geophys. Res. Lett., 39,

doi: 10.1029/2012GL052364.

Christian, J. R., M. A. Verschell, R. Murtugudde, A. J. Busalacchi, and C. R. McClain (2002), Biogeochemical modelling of the tropical Pacific Ocean. II: Iron biogeochemistry, Deep-Sea Res. Pt. II, 49, 545-565.

Church, J. A., P. U. Clark, A. Cazenave, J. M. Gregory, S. Jevrejeva, A. Levermann, M. A. Merrifield, G. A. Milne, R. S. Nerem, P. D. Nunn, A. J. Payne, W. T. Pfeffer, D. Stammer and A. S. Unnikrishnan (2013), Sea Level Change. In: Climate Change 2013: The Physical Science Basis. Contribution of Working Group I to the Fifth Assessment Report of the Intergovernmental Panel on Climate Change, edited by T. Stocher et al., Cambridge Univ. Press, Cambridge, U. K. and New York.

Coale, K. H., S. E. Fitzwater, R. M. Gordon, K. S. Johnson, and R. T. Barber (1996a), Control of community growth and export production by upwelled iron in the equatorial Pacific Ocean, Nature, 379, 621-624.

Coale, K. H., Johnson, K. S. Fitzwater, S. E. Gordon, R. M. Tanner, S. Chavez, F. P. Ferioli, L. Sakamoto, C. Rogers, P. Millero, F. Steinberg, P. Nightingale, P. Cooper, D. Cochlan, W. P. Landry, M. R. Constantinou, J. Rollwagen, G. Trasvina, A. Kudela, R. (1996b), A massive phytoplankton bloom induced by an ecosystem-scale iron fertilization experiment in the equatorial Pacific Ocean, Nature, 383, 495-501.

Collins, M., R. Knutti, J. Arblaster, J.-L. Dufresne, T. Fichefet, P. Friedlingstein, X. Gao, W. J. Gutowski, T. Johns, G. Krinner, M. Shongwe, C. Tebaldi, A. J. Weaver and M. Wehner (2013), Long-term Climate Change: Projections, Commitments and Irreversibility. In: Climate Change 2013: The Physical Science Basis.

Contribution of Working Group I to the Fifth Assessment Report of the Intergovernmental Panel on Climate Change, edited by Stocker, T. F. et al., Cambridge Univ. Press, Cambridge, U. K. and New York.

DiNezio, P. N., A. C. Clement, G. A. Vecchi, B. J. Soden, and B. P. Kirtman (2009), Climate response of the equatorial Pacific to global warming, J. Clim., 22, 4873-4892, doi: 10.1175/2009JCLI2982.1.

Fang, C. F., and L. X. Wu (2008), The role of ocean dynamics in tropical Pacific SST response to warm climate in a fully coupled GCM, Geophys. Res. Lett., 35, doi:10.1029/2007GL033097.

Fiedler, P. C. (2002), Environmental change in the eastern tropical Pacific Ocean: review of ENSO and decadal variability, Mar. Ecol. Prog. Ser., 244, 265-283.

Frierson, D. M. W., J. Lu, and G. Chen (2007), Width of the Hadley cell in simple and comprehensive general circulation models, Geophys. Res. Lett., 34, doi:10.1029/2007GL031115.

Gan, B., L. Wu, F. Jia, S. Li, W. Cai, H. Nakamura, M. A. Alexander, and A. J. Miller (2017), On the response of the Aleutian Low to greenhouse warming, J. Clim., 30, 3907-3925, doi: 10.1175/JCLI-D-15-0789.1.

Gorgues, T., C. Menkes, L. Slemons, O. Aumont, Y. Dandonneau, M. H. Radenac, S. Alvain, and C. Moulin (2010), Revisiting the La Niña 1998 phytoplankton blooms in the equatorial Pacific, Deep-Sea Res. Pt. I, 57, 567-576, doi: 10.1016/j.dsr.2009.12.008.

Gregory, J. M., et al. (2001), Comparison of results from several AOGCMs for global and regional sea-level change 1900-2100, Clim. Dyn., 18, 225-240.

Gruber, N. (2011), Warming up, turning sour, losing breath: ocean biogeochemistry under

global change, Philos. T. R. Soc. A., 369, 1980-1996.

Hartmann, D. L., A. M. G. Klein Tank, M. Rusticucci, L. V. Alexander, S. Brönnimann, Y. Charabi, F. J. Dentener, E. J., and D. R. E. Dlugokencky, A. Kaplan, B. J. Soden, P. W. Thorne, M. Wild and P. M. Zhai (2013), Observations: Atmosphere and Surface, In: Climate Change 2013: The Physical Science Basis. Contribution of Working Group I to the Fifth Assessment Report of the Intergovernmental Panel on Climate Change, edited by T. F. Stocker et al., Cambridge Univ. Press, Cambridge, U. K. and New York.

Hu, Y., L. Tao, and J. Liu (2013), Poleward expansion of the Hadley circulation in CMIP5 simulations, Adv. Atmos. Sci., 30, 790-795.

Ishii, M., and M. Kimoto (2009), Reevaluation of historical ocean heat content variations with time-varying XBT and MBT depth bias corrections, J. Oceanogr., 65, 287-299.

Jia, F., L. X. Wu, B. L. Gan, and W. J. Cai (2016), Global warming attenuates the tropical Atlantic-Pacific teleconnection, Sci. Rep., 6, doi: 10.1038/srep20078.

Jin, F. F. (1997), An equatorial ocean recharge paradigm for ENSO. Part II: A stripped-down coupled model, J. Atmos. Sci., 54, 830-847.

Johanson, C. M., and Q. Fu (2009), Hadley cell widening: model simulations versus observations, J. Clim., 22, 2713-2725.

Keeling, R. F., A. Kortzinger, and N. Gruber (2010), Ocean deoxygenation in a warming world, Annu. Rev. Mar. Sci., 2, 199-229.

Kirtman, B. P. (1997), Oceanic Rossby wave dynamics and the ENSO period in a coupled model, J. Clim., 10, 1690-1704.

Knutson, T. R., and S. Manabe (1995), Time-mean response over the tropical Pacific to

increased CO2 in a coupled ocean-atmosphere model, J. Clim., 8, 2181-2199.

Liddicoat, S., C. Jones, and E. Robertson (2013), CO2 emissions determined by HadGEM2-ES to be compatible with the representative concentration pathway scenarios and their extensions, J. Clim, 26, 4381-4397, doi: 10.1175/JCLI-D-12-00569.1.

Liu Z.-J., S. Minobe, Y. N. Sasaki and M. Terada (2016), Dynamical downscaling of future sea-level change in the western North Pacific using ROMS, J. Oceanogr., 72, 905-922, doi: 10.1007/s10872-016-0390-0.

Liu, F. K., Y. Y. Luo, J. Lu, and X. Q. Wan (2017), Response of the tropical Pacific Ocean to El Niño versus global warming, Clim. Dyn., 48, 935-956, doi: 10.1007/s00382-016-3119-2.

Liu, Z. Y. (1998), The role of ocean in the response of tropical climatology to global warming: The west-east SST contrast, J. Clim., 11, 864-875.

Lowe, J. A., and J. M. Gregory (2006), Understanding projections of sea level rise in a Hadley Centre coupled climate model, J. Geophys. Res., 111, doi:10.1029/2005JC003421.

Lu, J., G. A. Vecchi, and T. Reichler (2007), Expansion of the Hadley cell under global warming, Geophys. Res. Lett., 34, doi: 10.1029/ 2006GL028443.

Luo, Y. Y., J. Lu, F. K. Liu, and W. Liu (2015), Understanding the El Niño-like oceanic response in the tropical Pacific to global warming, Clim. Dyn., 45, 1945-1964.

Luo, Y. Y., Q. Y. Liu, and L. M. Rothstein (2009), Simulated response of North Pacific Mode Waters to global warming, Geophys. Res. Lett., 36, doi:10.1029/2009GL040906

Luo, Y. Y., and L. M. Rothstein (2011), Response of the Pacific Ocean circulation to

climate change, Atmos. Ocean, 49, 235-244.

Lyu, K., X. Zhang, J. A. Church, and J. Hu (2016), Evaluation of the interdecadal variability of sea surface temperature and sea level in the Pacific in CMIP3 and CMIP5 models, Int. J. Climatol., 36, 3723-3740, doi:10.1002/joc.4587.

Mackey, D. J., J. E. O'Sullivan, and R. J. Watson (2002), Iron in the western Pacific: a riverine or hydrothermal source for iron in the Equatorial Undercurrent?, Deep-Sea Res. Pt. I, 49, 877-893.

Martin, J. H., R. M. Gordon, and S. E. Fitzwater (1991), The case for iron, Limnol. Oceanogr., 36, 1793-1802.

McPhaden, M. J. (1993), TOGA-TAO and the 1991-93 El Niño-Southern Oscillation event, Oceanogr., 6, 36-44.

McPhaden, M. J. (1999), Genesis and evolution of the 1997-98 El Niño, Science, 283, 950-954.

Meehl, G. A., C. Covey, T. Delworth, M. Latif, B. McAvaney, J. F. B. Mitchell, R. J. Stouffer, and K. E. Taylor (2007), The WCRP CMIP3 multimodel dataset - A new era in climate change research, Bull. Am. Meteorol. Soc., 88, 1383-1394.

Meehl, G. A., W. D. Collins, B. A. Boville, J. T. Kiehl, T. M. L. Wigley, and J. M. Arblaster (2000), Response of the NCAR climate system model to increased CO2 and the role of physical processes, J. Clim., 13, 1879-1898.

Meehl, G. A., and W. M. Washington (1996), El Niño-like climate change in a model with increased atmospheric CO2 concentrations, Nature, 382, 56-60.

Meinshausen, M., Smith, S. J. Calvin, K. Daniel, J. S. Kainuma, M. L. T. Lamarque, J. F. Matsumoto, K. Montzka, S. A. Raper, S. C. B. Riahi, K. Thomson, A. Velders, G. J. M. van Vuuren, D. P. P. (2011), The RCP greenhouse gas concentrations

and their extensions from 1765 to 2300, Clim. Change, 109, 213-241.

Miller, R. L., G. A. Schmidt, and D. T. Shindell (2006), Forced annular variations in the 20th century Intergovernmental Panel on Climate Change Fourth Assessment Report models, J. Geophys. Res., 111, doi:10.1029/2005JD006323.

Mitrovica, J. X., N. Gomez, E. Morrow, C. Hay, K. Latychev, and M. E. Tamisiea (2011), On the robustness of predictions of sea level fingerprints, Geophys. J. Int., 187, 729-742.

Nicholls, R. J., S. E. Hanson, J. A. Lowe, R. A. Warrick, X. Lu, and A. J. Long (2014), Sea-level scenarios for evaluating coastal impacts, WIREs Clim. Change 2014, 5, 129-150, doi: 10.1002/wcc.253.

Oshima, K., Y. Tanimoto, and S.-P. Xie (2012), Regional patterns of wintertime SLP change over the North Pacific and their uncertainty in CMIP3 multi-model projections, J. Meteorol. Soc. Jpn., 90A, 385-396. doi:10.2151/jmsj.2012-A23.

Pardaens, A. K., J. M. Gregory, and J. A. Lowe (2010), A model study of factors influencing projected changes in regional sea level over the twenty-first century, Clim. Dyn. 36, 2015-2033.

Pedlosky, J. (1996), Ocean circulation theory, 453 pp., Springer, Berlin.

Peltier, W. R. (2004), Global glacial isostasy and the surface of the ice-age Earth: The ICE-5G (VM2) Model and GRACE, Annu. Rev. Earth Planet Sci., 32, 111-149.

Philander, S. G. H. (1981), The response of equatorial oceans to a relaxation of the trade winds, J. Phys. Oceanogr., 11, 176-189.

Previdi, M., and B. G. Liepert (2007), Annular modes and Hadley cell expansion under global warming, Geophys. Res. Lett., 34, doi:10.1029/2007GL031243.

R. J. Nicholls, S. H., C. Herweijer, N. Patmore, S. Hallegatte, J. Corfee-Morlot, Jean

Chateau, Robert Muir-Wood (2008), Ranking port cities with high exposure and vulnerability to climate extremes, OECD Environ. Working Pap. 1, 62 pp., Organ. for Econ. Coop. and Dev., Paris.

Rauthe, M., A. Hense, and H. Paeth (2004), A model intercomparison study of climate change-signals in extratropical circulation. Int. J. Clim., 24, 643-662.

Ryan, J. P., I. Ueki, Y. Chao, H. C. Zhang, P. S. Polito, and F. P. Chavez (2006), Western Pacific modulation of large phytoplankton blooms in the central and eastern equatorial Pacific, J. Geophys. Res.-Biogeo., 111, doi:10.1029/2005JG000084.

Sen Gupta, A., A. Ganachaud, S. McGregor, J. N. Brown, and L. Muir (2012), Drivers of the projected changes to the Pacific Ocean equatorial circulation, Geophys. Res. Lett., 39, doi:10.1029/2012GL051447.

Seo, H., and S. P. Xie (2011), Response and impact of equatorial ocean dynamics and tropical instability waves in the tropical Atlantic under global warming: A regional coupled downscaling study, J. Geophys. Res.-Oceans, 116, doi:10.1029/2010JC006670.

Slangen, A. B. A., M. Carson, C. A. Katsman, R. S. W. van de Wal, A. Köhl, L. L. A. Vermeersen, and D. Stammer (2014), Projecting twenty-first century regional sea-level changes, Clim. Change, 124, 317-332, doi:10.1007/s10584-014-1080-9.

Slemons, L. O., J. W. Murray, J. Resing, B. Paul, and P. Dutrieux (2010), Western Pacific coastal sources of iron, manganese, and aluminum to the Equatorial Undercurrent, Global. Biogeochem. Cy., 24, doi:10.1029/2009GB003693.

Sloyan, B. M., G. C. Johnson, and W. S. Kessler (2003), The Pacific cold tongue: A pathway for interhemispheric exchange, J. Phys. Oceanogr., 33, 1027-1043.

Sueyoshi, M., and T. Yasuda (2012), Inter-model variability of projected sea level changes

in the western North Pacific in CMIP3 coupled climate models, J. Oceanogr., 68, 533-543.

Sugimoto, S., K. Hanawa, T. Watanabe, T. Suga, and S. P. Xie (2017), Enhanced warming of the subtropical mode water in the North Pacific and North Atlantic. Nat. Clim. Change, 7, 656-658, doi: 10.1038/nclimate3371.

Suzuki, T., and M. Ishii (2011a), Regional distribution of sea level changes resulting from enhanced greenhouse warming in the Model for Interdisciplinary Research on Climate version 3.2, Geophys. Res. Lett., 38, doi:10.1029/2010GL045693.

Suzuki, T., and M. Ishii (2011b), Long-term regional sea level changes due to variations in water mass density during the period 1981-2007, Geophys. Res. Lett., 38, doi:10.1029/2011GL049326.

Taylor, K. E., R. J. Stouffer, and G. A. Meehl (2012), An overview of CMIP5 and the experiment design, Bull. Amer. Meteor. Soc., 93, 485-498, doi: 10.1175/BAMS-D-11-00094.1, doi: 10.1175/BAMS-D-11-00094.1.

Thomson, A. M., Calvin, K. V., Smith, S. J., Kyle, G. Page, Volke, April, Patel, Pralit, Delgado-Arias, Sabrina, Bond-Lamberty, Ben, Wise, Marshall A., Clarke, Leon E., Edmonds, James A., (2011), RCP4.5: a pathway for stabilization of radiative forcing by 2100, Clim. Change, 109, 77-94, doi:10.1007/s10584-011-0151-4.

Timmermann, A., S. McGregor, and F.-F. Jin (2010), Wind effects on past and future regional sea level trends in the Southern Indo-Pacific, J. Clim., 23, 4429-4437.

Vecchi, G. A., B. J. Soden, A. T. Wittenberg, I. M. Held, A. Leetmaa, and M. J. Harrison (2006), Weakening of tropical Pacific atmospheric circulation due to anthropogenic forcing, Nature, 441, 73-76, doi: 10.1038/nature04744.

Vecchi, G. A., and B. J. Soden (2007), Global warming and the weakening of the tropical

circulation, J. Clim., 20, 4316-4340, doi: 10.1175/JCLI4258.1.

Wada, Y., L. P. H. van Beek, F. C. Sperna Weiland, B. F. Chao, Y.-H. Wu, and M. F. P. Bierkens (2012), Past and future contribution of global groundwater depletion to sea-level rise, Geophys. Res. Lett. 39, doi:10.1029/2012GL051230.

Willis, J. K., and J. A. Church (2012), Climate change. Regional sea-level projection, Science, 336: 550-551.

Wittenberg, A. T. (2002), ENSO response to altered climates, Ph.D. thesis, 475 pp, Princeton Univ., Princeton, N.J.

Yin, J. (2012), Century to multi-century sea level rise projections from CMIP5 models, Geophys. Res. Lett., 39, doi:10.1029/2012GL052947.

Yin, J., S. M. Griffies, and R. J. Stouffer (2010), Spatial variability of sea level rise in twenty-first century projections, J. Clim., 23, 4585-4607.

Zebiak, S. E., and M. A. Cane (1987), A Model El-Nino Southern Oscillation, Mon. Wea. Rev., 115, 2262-2278.

Zhang, Q., Y. Guan, and H. J. Yang (2008), ENSO amplitude change in observation and coupled models, Adv. Atmos. Sci., 25, 361-366, doi: 10.1007/s00376-008-0361-5.

Zhang, X., J. A. Church, S. M. Platten, and D. Monselesan (2014), Projection of subtropical gyre circulation and associated sea level changes in the Pacific based on CMIP3 climate models, Clim. Dyn., 43, 131-144.